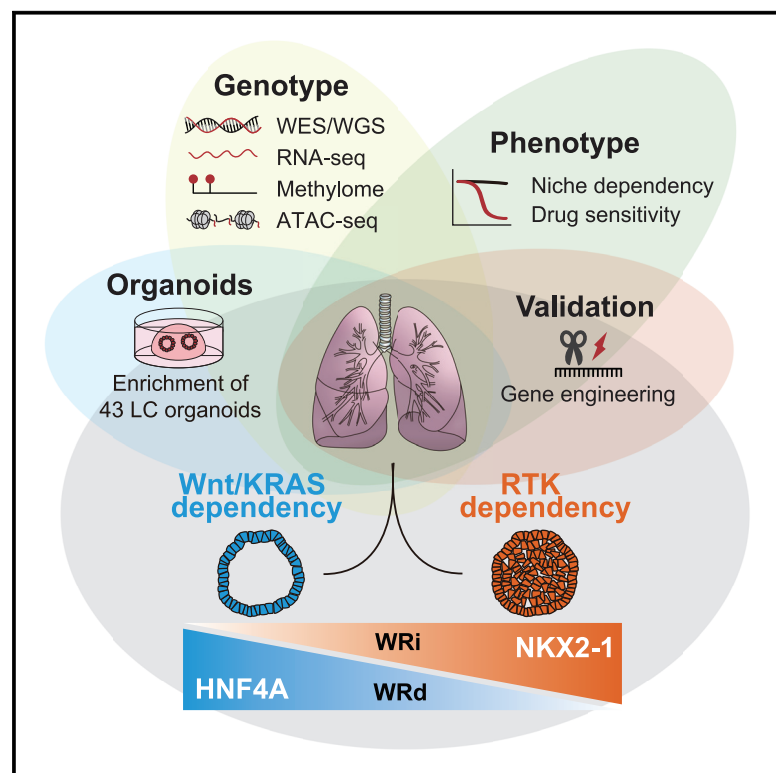


Genotype-phenotype mapping of a patient-derived lung cancer organoid biobank identifies NKX2-1-defined Wnt dependency in lung adenocarcinoma

Graphical abstract



Authors

Toshiki Ebisudani, Junko Hamamoto, Kazuhiro Togasaki, ..., Koichi Fukunaga, Hiroyuki Yasuda, Toshiro Sato

Correspondence

hiroyukiyasuda@a8.keio.jp (H.Y.), t.sato@keio.jp (T.S.)

In brief

Ebisudani et al. establish a patient-derived lung cancer organoid library encompassing all histologic types. Multi-omics and phenotypic analyses reveal that Wnt-dependent and -independent phenotypes in lung adenocarcinoma are defined by NKX2-1 expression. A stratification strategy based on NKX2-1 expression may predict the effect of Wnt-targeting therapy in human lung adenocarcinoma.

Highlights

- Establishment of 43 lung cancer organoid lines from patient tissues, sputum, blood
- Organoids reveal Wnt-dependent and -independent types in human lung adenocarcinoma
- Genetic engineering shows induction of Wnt independency by EGFR/Ras alterations
- Loss of NKX2-1 sensitizes human lung adenocarcinomas to Wnt-targeting therapy



Resource

Genotype-phenotype mapping of a patient-derived lung cancer organoid biobank identifies NKX2-1-defined Wnt dependency in lung adenocarcinoma

Toshiki Ebisudani,^{1,2} Junko Hamamoto,² Kazuhiro Togasaki,¹ Akifumi Mitsuishi,² Kai Sugihara,² Taro Shinozaki,² Takahiro Fukushima,² Kenta Kawasaki,¹ Takashi Seino,¹ Mayumi Oda,¹ Hikaru Hanyu,¹ Kohta Toshimitsu,¹ Katsura Emoto,³ Yuichiro Hayashi,³ Keisuke Asakura,⁴ Todd A. Johnson,⁵ Hideki Terai,² Shinnosuke Ikemura,² Ichiro Kawada,² Makoto Ishii,² Tomoyuki Hishida,⁴ Hisao Asamura,⁴ Kenzo Soejima,² Hidewaki Nakagawa,⁵ Masayuki Fujii,¹ Koichi Fukunaga,² Hiroyuki Yasuda,^{2,*} and Toshiro Sato^{1,6,*}

¹Department of Organoid Medicine, Keio University School of Medicine, Tokyo 160-8582, Japan

²Department of Pulmonary Medicine, Keio University School of Medicine, Tokyo 160-8582, Japan

³Division of Diagnostic Pathology, Keio University School of Medicine, Tokyo 160-8582, Japan

⁴Division of Thoracic Surgery, Keio University School of Medicine, Tokyo 160-8582, Japan

⁵Laboratory for Cancer Genomics, RIKEN Center for Integrative Medical Sciences, Yokohama 230-0045, Japan

⁶Lead contact

*Correspondence: hiroyukiyasuda@a8.keio.jp (H.Y.), t.sato@keio.jp (T.S.)

<https://doi.org/10.1016/j.celrep.2023.112212>

SUMMARY

Human lung cancer is a constellation of tumors with various histological and molecular properties. To build a preclinical platform that covers this broad disease spectrum, we obtained lung cancer specimens from multiple sources, including sputum and circulating tumor cells, and generated a living biobank consisting of 43 lines of patient-derived lung cancer organoids. The organoids recapitulated the histological and molecular hallmarks of the original tumors. Phenotypic screening of niche factor dependency revealed that EGFR mutations in lung adenocarcinoma are associated with the independence from Wnt ligands. Gene engineering of alveolar organoids reveals that constitutive activation of EGFR-RAS signaling provides Wnt independence. Loss of the alveolar identity gene *NKX2-1* confers Wnt dependency, regardless of EGFR signal mutation. Sensitivity to Wnt-targeting therapy can be stratified by the expression status of *NKX2-1*. Our results highlight the potential of phenotype-driven organoid screening and engineering for the fabrication of therapeutic strategies to combat cancer.

INTRODUCTION

Lung cancer (LC) is the leading cause of cancer-related deaths, accounting for approximately 1.8 million annual mortalities or 18% of all cancer-related deaths worldwide.¹ LC is a heterogeneous disease that broadly encompasses two major categories: small cell LC (SCLC) and non-SCLC. The latter mainly consists of lung adenocarcinoma (LUAD), lung squamous cell carcinoma (LUSC), and a rare histologic subtype, large cell neuroendocrine carcinoma (LCNEC). Of these subtypes, chemotherapy for LUAD, which dominates approximately 60% of all LC cases and is responsible for the majority of LC-related deaths, has been rapidly evolving owing to the discovery of molecular targets² and the development of targeted drugs that show clinical activity. The list of such druggable molecular targets, including *EGFR*, *KRAS*^{G12C}, and *BRAF*^{V600E} mutations, and *ALK*-, *ROS1*-, *RET*-, and *NTRK*-translocations,^{3–6} has continued to expand owing to large-scale sequencing efforts. Nevertheless, approximately one-half of LUAD cases are devoid of genetic abnormalities that are currently druggable, highlighting

the limitation of genomics-guided precision oncology that selects chemotherapy regimens based on the genomic profile of the patient tumor.^{7,8}

Although targeted therapy generally co-opts cancer dependencies, pathways and modules that are integral to cancer growth or survival may not be captured by molecular profiling and require biological analysis of patient tumors. Functional investigation of human cancers has traditionally relied on cancer cell lines, but their poor capacity to recapitulate clinical tumors often undermines their usefulness as preclinical models. Furthermore, the requirement for serum in cell line culture obscures the cell-intrinsic dependency on the microenvironment or niche, despite its relevance to cancer addiction and potential as a therapeutic target. Cell line culture also does not support the long-term propagation of normal counterpart cells, including the proximal squamous airway epithelium and the distal lung alveolar epithelium. To overcome these limitations, recent studies have applied organoid technology to pulmonary biology and medicine and established organoids from patient-derived LC tissues, and normal airway and alveolar epithelia.^{9–16} Although these studies



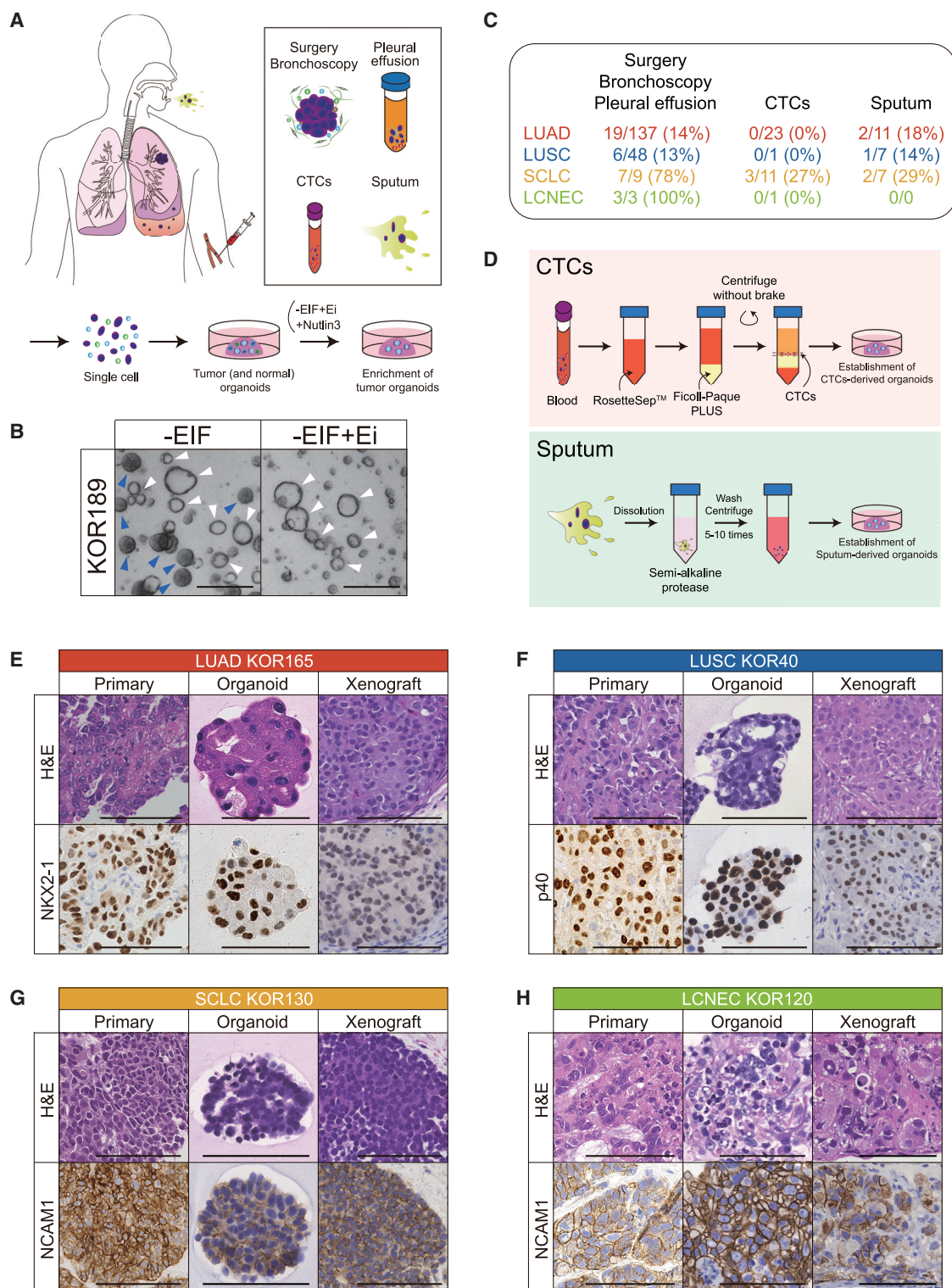


Figure 1. Establishment of a patient-derived LC organoid library

(A) Overview of the procedures used to establish LC organoid library. LC tissues were obtained by surgery, bronchoscopy, pleural effusion, CTCs, and sputum, and treated with Nutlin-3 and pan Ei for the enrichment of LC organoids.

(B) Representative images before and after an elimination of contaminating normal airway organoids with Ei. The organoid culture initially consisted of normal airway (blue arrowheads) and LC (white arrowheads) organoids (left). LC organoids selectively expanded in the presence of Ei (right).

(legend continued on next page)

consistently demonstrated that patient-derived LC organoids phenocopied genetic alterations and the drug sensitivity of patient LCs, the dependency of patient-derived LC organoids on niche signals, including the highly clinically relevant epidermal growth factor receptor (EGFR)-RAS pathway, remains to be thoroughly assessed. Furthermore, considering that tumors with identical driver mutations can exhibit variable phenotypes, including histological traits and sensitivity to chemotherapy, the causality of putative genotype-phenotype associations in LC organoids should be verified through genetic perturbation of normal human lung organoids.

To overcome the current drawbacks of human LC research, we established an LC organoid library consisting of 43 patient-derived LC organoids. We carried out integrative characterization of organoids from molecular and phenotypic viewpoints using multi-omics analysis, niche dependency profiling, and CRISPR-Cas9-based gene engineering. Our results uncover distinct molecular routes to lung carcinogenesis and provides previously unappreciated links between the epigenetic status and therapeutic vulnerability in human LC.

RESULTS

Establishment of a patient-derived LC organoid library

To establish a living and accessible platform for human LC research, we sought to create a patient-derived LC organoid library that encompasses the diverse molecular, histological, and phenotypic spectra of human LC. With this aim, we isolated LC cells from surgical specimens, bronchoscopy biopsies, and pleural effusions obtained from patients with LC (Table S1). Harvested LC cells were first expanded under previously reported conditions^{10,13,17} (Figure 1A), which contained EGF/insulin growth factor-1/fibroblast growth factor-2 (EIF), Noggin, transforming growth factor (TGF)- β inhibitor, and Wnt-3A/R-spondin (WR). As previously shown,⁹ these conditions are optimized for the normal epithelium and often allowed normal airway epithelium to outgrow from LC tissues and subsequently overwhelm LC organoids. To prevent the outgrowth of normal airway organoids, we exploited the high prevalence of TP53 and ERBB pathway mutations in human LC. First, supplementation with Nutlin-3 (an MDM-2 inhibitor) efficiently eliminated outgrowing normal organoids and enriched TP53-mutated LC organoids,⁹ but it may potentially eradicate LC organoids without TP53 mutation. To circumvent this drawback, we prepared a second cancer-selective condition that halts ERBB signaling by removing EIF and adding a pan-ERBB inhibitor (Ei), given that normal airway and alveolar organoids cannot grow in the presence of Ei. These cancer-selective culture conditions enabled the estab-

lishment of organoid cultures consisting purely of LC organoids with cancer-relevant mutations (described in the next section) (Figure 1B). As a result, two LC organoid lines carried wild-type TP53 and could be purified using only the current protocol. The establishment efficiency of LC organoids varied among histological types, ranging from only 13% to 14% in LUAD and LUSC to 78% in SCLC (Figure 1C). We could also establish organoids from LCNEC tissues at a take rate of 100%, although the sample size was small. The modest organoid establishment efficiency of LUAD and LUSC was consistent with previous reports.^{9,13,15} All established LC organoids underwent stable propagation for at least five passages and could be recovered on demand from frozen stocks.

To cover a broader range of interpatient heterogeneity, we sought to establish LC organoids from patient materials obtained using minimally invasive sampling approaches (Figure 1D). We established LC organoids from sputum samples. From the sputa of 25 patients who had already been diagnosed with LC by sputum cytology, we established 5 sputum-derived LC organoid lines. We also collected blood-circulating tumor cells (CTCs) from 36 donors with LC and successfully established three lines of CTC-derived LC organoids (Figure 1C). All successful cases were of SCLC origin, likely reflecting the higher CTC count in SCLC patients than in non-SCLC patients.¹⁸ Altogether, we established 43 LC organoid lines that encompassed four major histological types (21 LUAD, 7 LUSC, 12 SCLC, and 3 LCNEC organoids).

To validate whether LC organoids preserve the original histological characteristics, we transplanted LC organoids into immunodeficient mice and compared their histopathology with that of the original clinical tumors. The pathological appearance and the expression of histological subtype markers, NKX2-1 (TTF-1) for LUAD, p40 for LUSC, and NCAM1 for SCLC and LCNEC, were concordant across the primary tissues, *in vitro* organoids, and xenografts (Figures 1E–1H and S1A–S1D). The mRNA expression of subtype markers in organoids also corresponded with their protein expression in parental tumors (Figure S1E). These results confirm the cancer origin of LC organoids and their preservation of histopathological identity during organoid derivation.

The molecular profile of LC organoids reflects histological subtypes

To investigate genomic abnormalities in LC organoids, we conducted whole-exome sequencing and whole-genome sequencing (Table S2). All LC organoids harbored TP53 mutations and/or EGFR-RAS signal alterations, indicative of their cancer origin (Figures 2A, S2A and S2B). Capillary immunoassay confirmed the lack of TP53 protein expression and its induction

(C) Breakdown of the LC organoid library based on histology and sampling methods. The probability of successful organoid establishment is shown.

(D) Establishment of CTCs- (top) or sputum-derived (bottom) LC organoids.

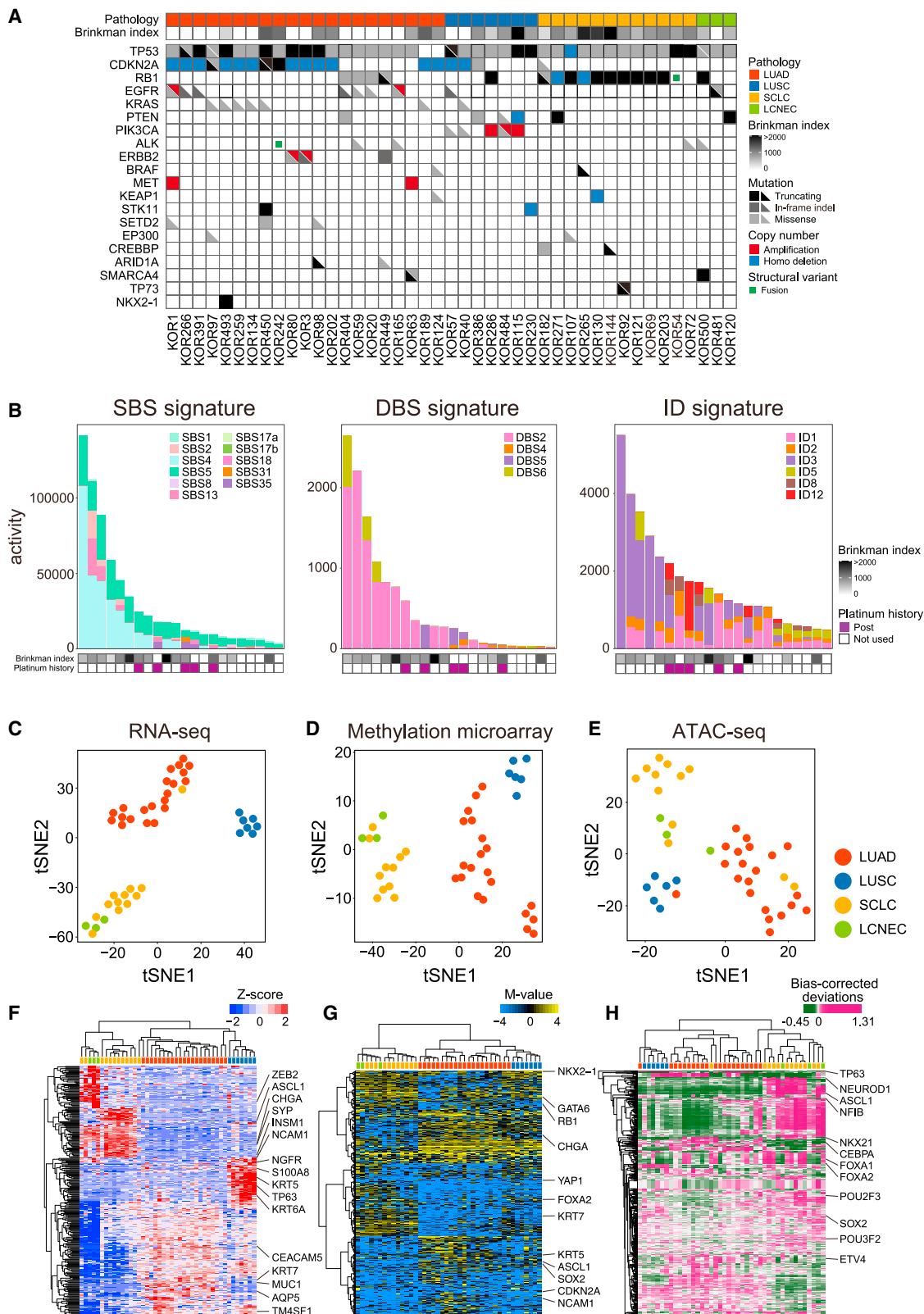
(E) Representative hematoxylin and eosin (H&E) and NKX2-1 staining of the parental tumor (left), organoids (middle), and organoid xenografts (right) of a LUAD organoid line (KOR165).

(F) Representative hematoxylin and eosin (H&E) and p40 staining of the parental tumor (left), organoids (middle) and organoid xenografts (right) of a LUSC organoid line (KOR40).

(G) Representative H&E and NCAM1 staining of the parental tumor (left), organoids (middle) and organoid xenografts (right) of an SCLC organoid line (KOR130).

(H) Representative H&E and NCAM1 staining of the parental tumor (left), organoids (middle) and organoid xenografts (right) of an LCNEC organoid line (KOR120).

Scale bar, 100 μ m (E, F, G, H), 200 μ m (B). See also Figure S1.



(legend on next page)

following nutlin-3 treatment in TP53-null LC organoids (Figure S2C). LC organoids showed genetic mutations, copy number alterations, and aneuploidy, with a pattern similar to that found in clinical specimens (Figures 2A and S2D).^{2,19–21} For example, EGFR-RAS signal alterations were exclusively detected in non-SCLC organoids. Compound TP53 and RB1 mutations were prevalent in SCLC and LCNEC organoids. To understand the mutational process underlying lung carcinogenesis, we next examined mutational signatures that reflect various mutational processes including extrinsic and intrinsic processes.^{22,23} LC organoids derived from patients with a smoking history exhibited mutational signatures associated with tobacco smoking (SBS-4, DBS-2, and ID-3) (Figure 2B).²² Platinum signatures (SBS-35 and DBS-5) were found in LUAD organoids derived from three of five patients who had been treated with platinum-based chemotherapy. APOBEC signatures (SBS-2 and -13) were present in a fraction of LUAD and LUSC organoids.²⁴

To gain a panorama of gene expression and epigenetic signatures in LC organoids, we carried out RNA sequencing, methylation microarray, and assay for transposase-accessible chromatin with high-throughput sequencing (ATAC-seq) analyses (Tables S3–S5). These analyses consistently distinguished LC organoids according to their histological subtypes (Figures 2C–2E). Unsupervised clustering analysis further revealed gene programs specific to each histological subtype. LUAD organoids showed high expression levels of *KRT7*, and active *NKX2-1* and *FOXA2*. LUSC organoids expressed *KRT5* and *NGFR*, and their accessible genomic regions were enriched with TP63 motifs. SCLC and LCNEC organoids expressed *NCAM1* and showed enrichment of *ASCL1* and *NEUROD1* motifs (Figures 2F–2H). Together, the multi-omics data of LC organoids highlighted the genetic programs linked with histological subtypes, independent of the surrounding environment.

LC histologic subtypes correlate with EGFR pathway dependency and drug sensitivity

To investigate genotype-phenotype correlations in LC organoids, we focused on the relationship between their dependency on biological niche factors and genetic alterations (Figure 3A). Considering the prevalent EGFR pathway mutations in LCs, we first analyzed the dependency of LC organoids on the EGF-relevant niche. One caveat of this assay is that the presence of serum in organoid culture medium potentially activates receptor tyrosine kinases and hinders an accurate assessment of niche factor dependency. To avoid this issue, we used an Afamin-stabilized serum-free Wnt-3A conditioned medium. Under serum-free culture conditions, normal alveolar organoids are strictly dependent on EIF.^{10,14,25} Receptor-level alterations, such as

EGFR and *ERBB2* mutations or alterations, enabled EIF-independent growth, whereas mutations or alterations in downstream molecules, including *KRAS* and *BRAF* mutations or alterations, and *EML4-ALK* fusion, conferred Ei resistance (Figures 3A and 3B). Notably, one LUAD organoid line was devoid of EGFR-RAS signal mutations and alterations, but exhibited EIF independence, presumably because of as-yet-unknown (epi-) genetic mechanisms (Figure 3A).

In contrast with LUAD, LUSC organoids were characterized by *PIK3CA* or *PTEN* mutations or alterations, instead of EGFR-RAS signal alterations (Figures S3A and S3B). LUSC organoids with PI3K signal alterations invariably showed EIF-independent growth, suggesting tropism for PI3K signal activation in gaining EIF independence. SCLC and LCNEC organoids were devoid of both EGFR-RAS and PI3K signal alterations, but grew independent of EIF (Figures S3A, S3C, and S3D). Such EIF independence that genetics cannot define is reminiscent of similar genotype-phenotype associations in gastroenteropancreatic neuroendocrine neoplasm organoids.²⁶

These results suggest that the effectiveness of molecularly targeted therapies in organoids can be predicted from their genotypes. To probe this notion, we investigated the therapeutic effect of EGFR-RAS signal perturbation in LUAD organoids. An immunoassay revealed a correlation between ERK phosphorylation, indicative of active EGFR-RAS signaling, and EIF independence and Ei resistance (Figure 3C). Ei blocked ERK activation in all but two LUAD organoid lines with EGFR alterations derived from tumors that were clinically refractory to EGFR-targeting therapy. A variety of EGFR-RAS signaling abnormalities in our LUAD organoids provided an opportunity to test the effect of clinically relevant targeted therapies. Organoid testing confirmed the genotype-specific effect of the FDA-approved drugs sotorasib (*KRAS*^{G12C} inhibitor), dabrafenib (*BRAF*^{V600E} inhibitor), and alectinb (*ALK* inhibitor) on LUAD organoids (Figures 3D–3F). The growth-inhibitory effect of these agents coincided with the inactivation of ERK (Figures 3G–3I). These data highlight a robust correlation between genetic alterations in EGFR-RAS signaling and therapeutic vulnerability in LC organoids.

LUAD consists of WNT-dependent and -independent subtypes

In contrast with the EGFR-RAS signaling pathway, the role of other niche signals in LC biology remains unknown. Thus, we examined how the activation of Wnt, bone morphogenetic protein (BMP), and TGF- β signaling affects the growth of LC organoids (Figure S4A). Stimulation with TGF- β 1 and BMP4 blunted the growth of LC organoids, indicating that the anti-proliferative effect of TGF- β /BMP signaling is intact in LC. Notably,

Figure 2. The molecular profile of LC organoids reflects histological subtypes

- (A) Histological subtype (pathology), brinkman index and genetic alterations of all organoid lines in LC organoid library.
 (B) Mutational signatures of LC organoids. SBS signatures (left), DBS signatures (middle), and ID signatures (right) are shown.
 (C–E) t-Distributed stochastic neighbor embedding (tSNE) visualization of the transcriptome (C), methylome (D), and ATAC-seq (E) data of LC organoid library using top eight principal components (perplexity = 8).
 (F) Hierarchical clustering of LC organoid library using differentially expressed genes (false discovery rate <25% and fold change >3 in any of the four pathologies).
 (G) Hierarchical clustering of LC organoid library using probes that were variably methylated (M-value variance >5) among the four histological subtypes.
 (H) Hierarchical clustering of LC organoid library using transcription factors with a variable motif enrichment (bias corrected deviation variance >2.25) among the four subtypes. See also Figure S2.

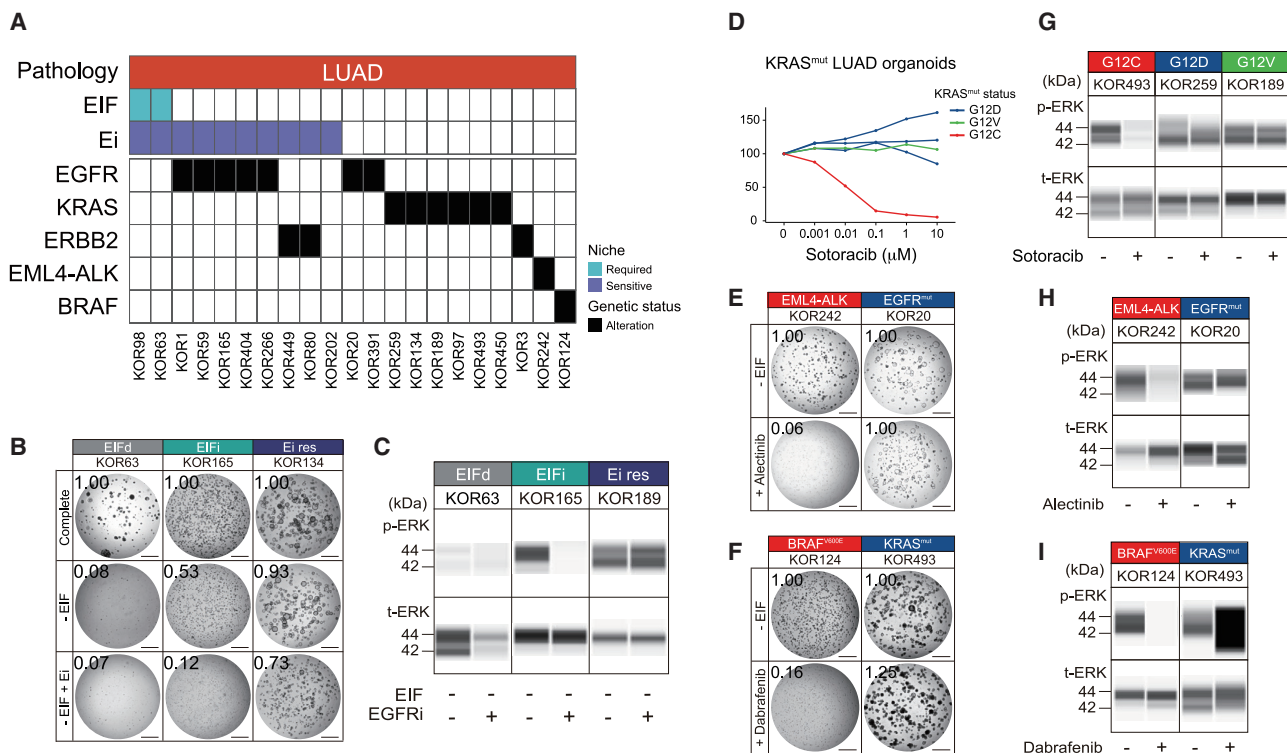


Figure 3. LC histologic subtypes correlate with EGFR pathway dependency and drug sensitivity

(A) EIF dependency, Ei sensitivity, and receptor tyrosine kinase (RTK) pathway-related genetic alterations in LUAD organoids. (B) Growth of EIF-dependent (EIFd), EIF-independent (EIFi), and Ei-resistant (Ei res) LUAD organoids in the indicated conditions. The mean organoid area relative to that of the complete condition with EIF is shown. (C) Total and phospho-ERK expression with or without Ei treatment in EIFd (left), EIFi (middle), and Ei res (right) LUAD organoids. (D) Dose-response curves of *KRAS*^{G12C} (n = 1), *KRAS*^{G12D} (n = 3), and *KRAS*^{G12V} (n = 1) LUAD organoids treated with sotorasib. (E and F) The effect of alectinib (E) or dabrafenib (F) on the growth of organoid lines with (left) or without (right) *EML4-ALK* fusion (E) or *BRAF*^{V600E} mutation (F). The mean organoid area relative to that of the control condition (–EIF) is shown. (G) Total and phospho-ERK expression in *KRAS*^{G12C} (left), *KRAS*^{G12D} (middle), and *KRAS*^{G12V} LUAD organoid (right) after sotorasib treatment. (H and I) Total and phospho-ERK expression in organoids with (left) or without (right) *EML4-ALK* fusion (H) or *BRAF*^{V600E} mutation (I) after alectinib (H) or dabrafenib (I) treatment. Scale bar, 1 mm (B, E, F). See also Figure S3.

approximately one-half of the LUAD and LUSC organoid lines showed resistance to BMP4. Given the lack of mutations relevant to BMP signaling, these organoid lines were considered to have acquired BMP resistance through non-genetic mechanisms.

Next, we determined the dependency of LC organoids on WR. Similar to BMP/TGF- β signaling, Wnt signaling mutations were absent in LC organoids, except in one LCNEC organoid line that harbored homozygous *APC* mutations. The xenograft of this LCNEC organoid line showed nuclear localization of β -catenin, suggesting constitutive Wnt activation (Figure S4B). We previously showed that human cancers carry over the dependence on stem cell niche factors from the tissue of origin, but often acquire niche independence through (epi)genetic alterations along with disease progression.^{27,28} Consistent with this concept and the WR independence of the airway epithelium,¹⁴ LUSC organoids invariably were WR independent (WRi). SCLC and LCNEC were also independent of WR, which may explain their origin in airway epithelium. Alternatively, they may have originated from WR-dependent (WRd) cells and acquired WR independence

through neuroendocrine reprogramming.²⁶ Given the requirements of WR in alveolar organoids, LUAD organoids were expected to be WRd. Indeed, one-third of LUAD organoids showed WR dependency (Figures 4A and 4B). Technically, these WRd LUAD organoids were dependent on endogenous Wnt ligands as they expressed Wnt ligands (Figures 4C and 4D) and were sensitive to Wnt-targeting with a porcupine inhibitor (described in a later section). R-spondin stabilizes Wnt receptors, but cannot activate Wnt signaling without Wnt ligands. Alveolar and LUAD organoids invariably expressed endogenous Wnt ligands and were sensitive to C59 treatment, indicating their dependency on both (endogenous) Wnt and R-spondin. Taken together, our results indicated that one-third of LUAD organoids inherited WR dependency from their cell of origin, yet the other LUAD organoids have somehow acquired WR independence.

EGFR-RAS signal alteration renders alveolar organoids Wnt independent

The heterogeneity of WR requirements among LUADs prompted us to explore the mechanism by which LUAD organoids acquired

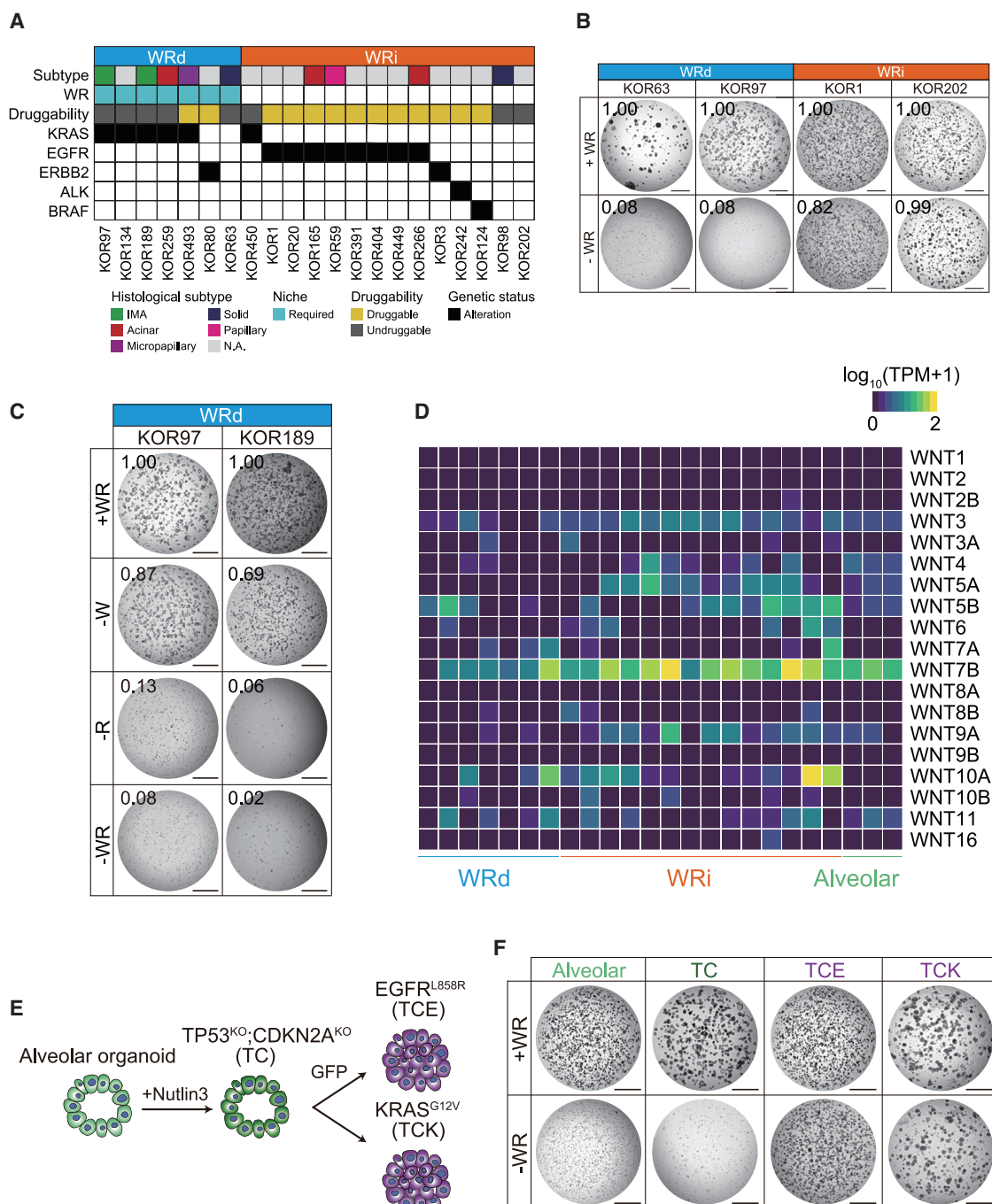


Figure 4. LUAD consists of WNT-dependent and -independent subtypes

(A) Histological subtype, WR dependency, drugability, and receptor tyrosine kinase (RTK) pathway genetic alterations in LUAD organoids.
 (B) Representative images of WRd (left) and WRi LUAD organoids cultured with (top) or without (bottom) WR. The mean organoid area relative to that of the +WR condition is shown.
 (C) Representative bright-field images of WRd organoids cultured with indicated conditions. Organoid area relative to the +WR condition is shown.
 (D) Transcript expression ($\log_{10}[\text{TPM}+1]$) of the indicated Wnt ligand genes in WRd, WRi, and normal alveolar organoids.
 (E) The strategy for genetically engineering normal alveolar organoids.
 (F) Representative images of normal alveolar, TC, TCE, and TCK organoids cultured with (top) or without (bottom) WR. Scale bar, 1 mm (B, C, F). See also Figure S4.

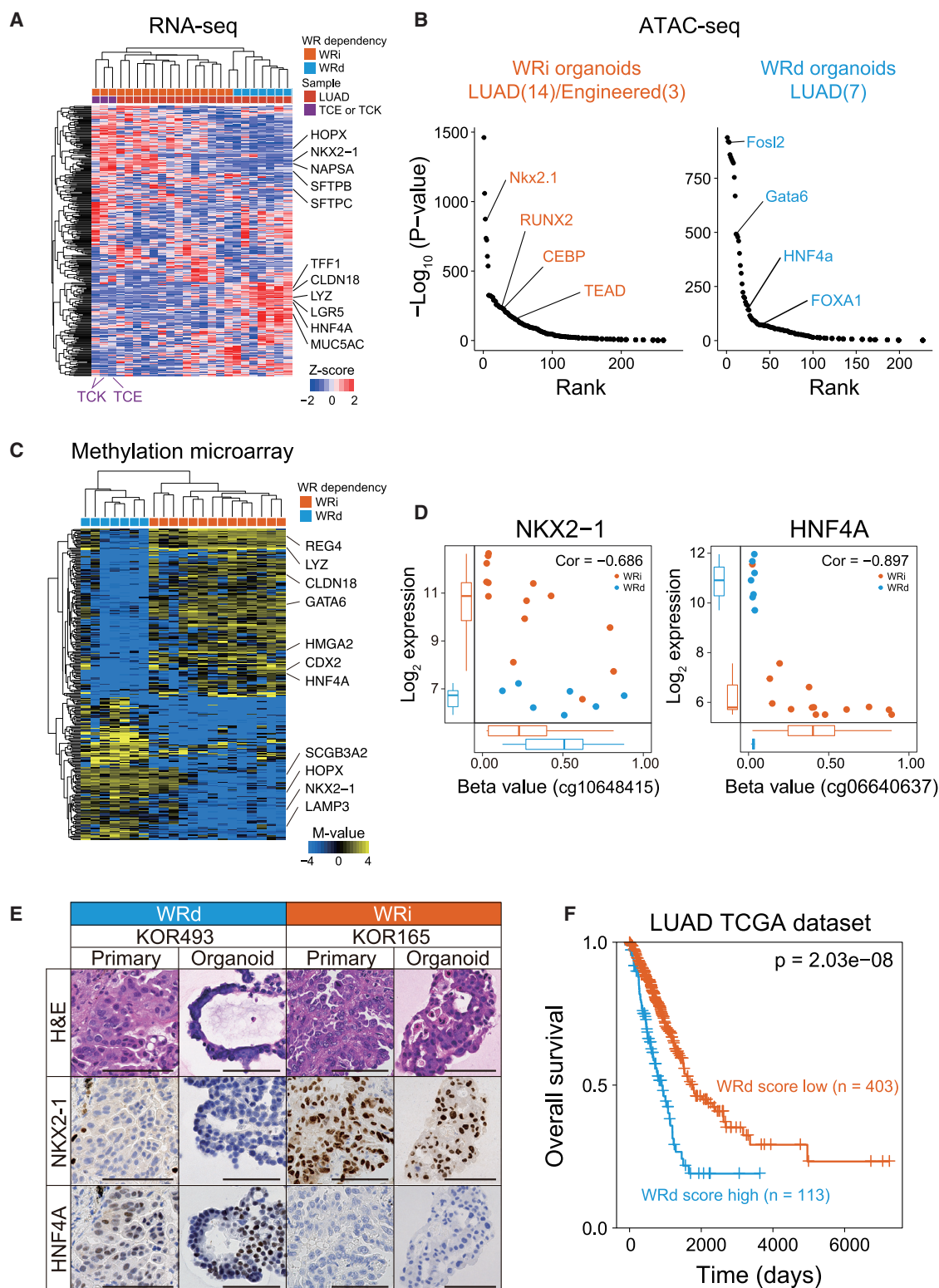


Figure 5. WR dependency of LUAD organoids is associated with lineage switching

(A) Hierarchical clustering of 21 LUAD and genetically engineered normal alveolar engineered organoids (2 TCK and 1 TCE) using variably expressed genes (variance >4).

(legend continued on next page)

the WRi phenotype. Notably, the WRi and WRd phenotypes were associated with *EGFR* and *KRAS* mutations, respectively (Figures 4A and 4B). To prospectively test this association, alveolar organoids were infected with lentiviruses expressing mutant *KRAS* or *EGFR*. Normal alveolar organoids underwent cell-cycle arrest after the induction of mutant *KRAS* or *EGFR*, presumably because of oncogenic senescence. To circumvent this issue, we first performed a double knockout (KO) of *TP53* and *CDKN2A*, genes recurrently inactivated in LUAD, on normal alveolar organoids using CRISPR/Cas9 (Figure 4E). Sanger sequencing validated legitimate gene disruption in the *TP53/CDKN2A*-KO (TC) organoids (Figure S4C). TC organoids tolerated the overexpression of mutant *KRAS* or *EGFR*, generating TCK or TCE organoids, respectively. EIF withdrawal ceased the proliferation of the original normal alveolar organoids, whereas TCK and TCE organoids continued to propagate and maintained ERK phosphorylation, indicating constitutive activation of the *EGFR*-RAS pathway (Figures S4D and S4E). Ei treatment blocked ERK activation in TCE organoids, but not in TCK organoids (Figure S4E). Intriguingly, TCE and TCK organoids gained the WRi phenotype, in contrast with the original TC organoids that retained WR dependence (Figure 4F). We confirmed this genotype-phenotype association using engineered organoid lines derived from an independent donor (Figure S4F). These results validated the association between the WRi phenotype and *EGFR* mutations. However, the WRi phenotype observed in the TCK organoids conflicts with the observation that most *KRAS*-mutated LUAD organoids were WRd.

WR dependency of LUAD organoids is associated with lineage switching

The phenotypic gap between the TCK-engineered WRi organoids and *KRAS*-mutant WRd LUAD organoids prompted us to explore whether molecular abnormalities other than genetic mutations are responsible for WR independence. Transcriptome analysis revealed a stark difference in the gene expression patterns between WRd LUAD organoids, WRi LUAD, and engineered TCE/TCK organoids. Interestingly, WRd organoids lost the expression of lung alveolus markers, such as *NKX2-1*, *SFTPB*, *SFTPC*, and *NAPSA*, but instead expressed genes associated with the gut lineage, including *TFF1*, *LYZ*, *LGR5*, *HNF4A*, and *GATA6* (Figure 5A). To further explore the molecular lesions responsible for altered lineage identity, we performed epigenetic analyses. ATAC-seq analysis delineated the aberrant activity of transcription factors, characterized by the de-enrichment of *NKX2-1* and enrichment of *GATA6*, *HNF4A*, and *FOXA1* activities in WRd organoids (Figures 5B,

S5A, and Table S6). Methylation micro-array analysis further confirmed similar alteration patterns in WRd organoids (Figures 5C and 5D). WRd organoids showed DNA methylation at the *NKX2-1* gene locus and DNA demethylation at the gene loci of gut transcription factors such as *HNF4A* (Figure S5B). One WRd LUAD organoid line (KOR493) carried a homozygous *NKX2-1* truncating mutation (Figure 2A), corroborating the relationship between *NKX2-1* loss and WR dependence. Immunohistochemistry confirmed similar patterns of lineage factor expression in parental tissues (Figure 5E). The expression of genes enriched in WRd organoids was significantly associated with inferior overall survival in the TCGA LUAD dataset (Figures 5F and S5C). Notably, the KOR450 LUAD organoid line harbored a *KRAS* mutation, but was independent of WRi (Figure 4A). In contrast with the other lines, KOR450 highly expressed *NKX2-1*, but not gut lineage transcription factors, indicating the preservation of the lung alveolar program. Taken together, these results suggest that the induction of the WRi phenotype by *EGFR*-RAS pathway mutations requires conservation of lung alveolar identity.

WNT independence in LUAD requires *NKX2-1*

Next, we asked whether LUAD organoids incur WR dependency upon the loss of lung alveolar identity. To this end, we introduced sgRNA targeting *NKX2-1* into three lines of *NKX2-1*⁺ WRi LUAD organoids (Figure 6A). Capillary immunoassays confirmed legitimate *NKX2-1* KO (Figures 6B and S6A). *NKX2-1* KO downregulated *NKX2-1* target genes, including *NAPSA*, *SFTPD*, *LAMP3*, and *LPCAT1* (Figure 6C). ATAC-seq confirmed the loss of *NKX2-1* transcriptional activity in *NKX2-1* KO organoids (Figure S6B). Interestingly, *NKX2-1* KO rendered all tested WRi LUAD organoid lines dependent on WR (Figures 6D and S6C). To confirm whether *NKX2-1* expression affects WR dependency, we investigated the effect of *NKX2-1* overexpression on *NKX2-1*[−] WRd LUAD organoids using a doxycycline (Dox)-inducible *NKX2-1* expression vector (Figure 6E). Capillary immunoassays confirmed *NKX2-1* expression after a 7-day Dox treatment (Figures 6F and S6D). Transcriptome and ATAC-seq analyses confirmed increased *NKX2-1* expression and activity after a 2-month Dox treatment (Figures 6G and S6E). Although WR withdrawal from the culture abrogated the growth of the engineered WRd LUAD organoids, Dox treatment rescued their growth and provided robust WR independence (Figures 6H and S6F). Collectively, these results indicate that *EGFR*-RAS mutations and *NKX2-1* expression coordinately induce the WRi phenotype in lung alveolar organoids.

(B) Transcription factors ranked according to the motif enrichment in WRi (14 LUAD and 3 engineered) (left) and WRd (7 LUAD organoids) (right) versus the other subtype.

(C) Hierarchical clustering of LC organoids using differentially methylated genes (M-value false discovery rate <10% and fold change >3) between WRd (n = 7) and WRi (n = 14) LUAD organoids.

(D) Negative correlations between the normalized gene expression and gene methylation beta value of the indicated probes for *NKX2-1* (left) and *HNF4A* (right). Pearson's correlation coefficients are shown.

(E) Representative hematoxylin and eosin (H&E), *NKX2-1*, and *HNF4A* staining of WRd (left) and WRi (right) organoids, together with their parental clinical tissues (left).

(F) The prognostic value of a high (blue) or low (orange) expression of WRd signature genes in the TCGA LUAD dataset. The tumors were divided according to the expression of the genes enriched in WRd LUAD organoids, and the difference in the overall survival was analyzed using the Kaplan-Meier method and log rank test. Scale bar, 100 μ m (E). See also Figure S5.

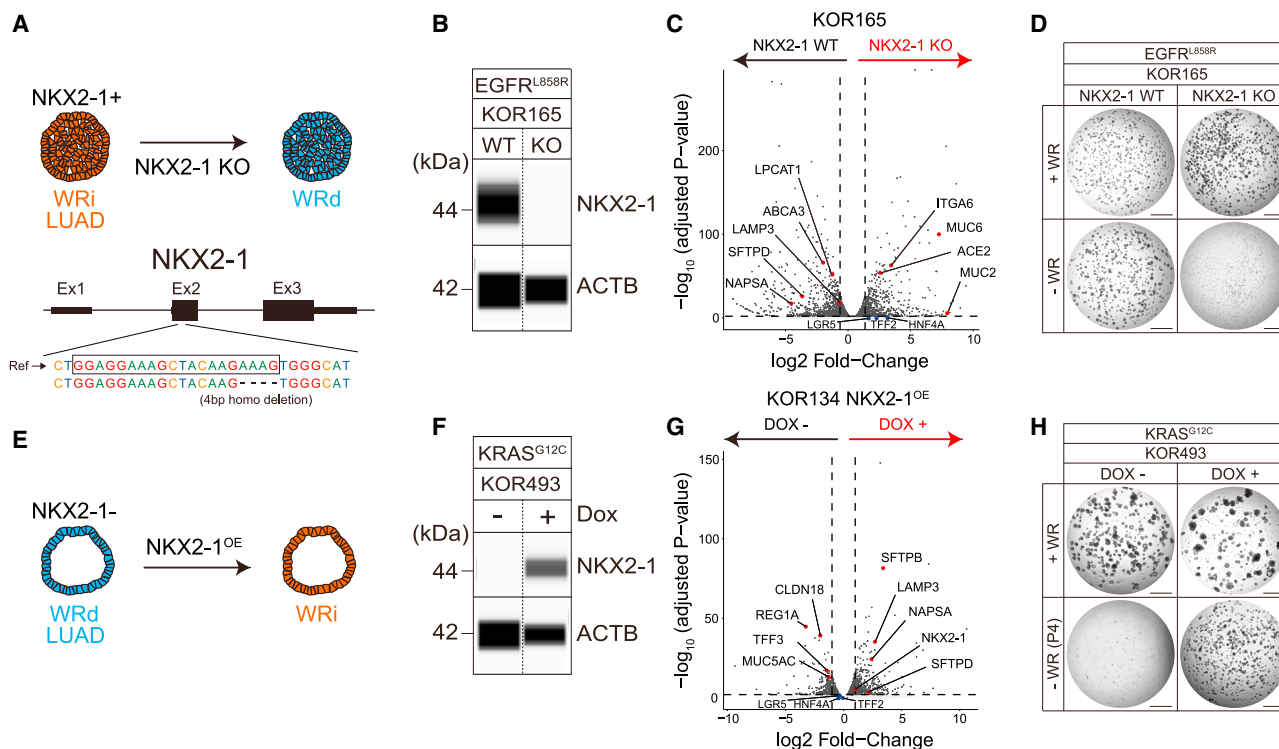


Figure 6. Wnt independence in LUAD requires NKX2-1

(A) *NKX2-1* KO in WRI LUAD organoids (top). KO confirmation by Sanger sequencing (bottom). Black frames show sgRNA targets.
(B) An immunoblot demonstrating the loss of NKX2-1 by *NKX2-1* KO.
(C) Comparison of the transcriptome between *NKX2-1*^{WT} and *NKX2-1*^{KO} KOR165 organoids (technical duplicate). Representative genes are highlighted in red. Dotted lines show log₂ (fold change) values of 1 and -1.
(D) The growth of *NKX2-1* WT and KO KOR165 organoids in the presence (top) or absence (bottom) of WR.
(E) Dox-inducible NKX2-1 overexpression in a WRd LUAD organoids.
(F) Immunoblot of Dox-induced NKX2-1. Organoid lysates were collected after a 7-day Dox treatment for Dox + organoids.
(G) Comparison of the transcriptome between Dox-treated (DOX+) and -untreated (DOX-) KOR134 NKX2-1^{OE} organoids (technical duplicate). Representative genes are highlighted in red. Dotted lines show log₂ (fold change) values of 1 and -1. The organoids were cultured with or without Dox for 2 months.
(H) The growth of NKX2-1^{OE} KOR493 LUAD organoids cultured with or without DOX in the presence (top) or absence (bottom, passage 4) of WR. Scale bar, 1 mm (D, H). See also Figure S6.

Therapeutic targeting of Wnt in WRd LUAD

Finally, we examined whether targeting Wnt signaling could provide a therapeutic option for the treatment of LUAD. We first enabled the conditional inactivation of Wnt signaling in LUAD organoids using Dox-inducible overexpression of dominant-negative TCF4 (dnTCF4).²⁹ Upon Dox treatment, the engineered organoids underwent strong dnTCF4 induction and downregulation of Wnt target genes such as *LGR5*, *AXIN2*, and *MYC* (Figures S7A and S7B). Consistent with the inactivation of Wnt signaling, Dox treatment also blocked the proliferation of WRd LUAD organoids (Figure S7C). dnTCF4 overexpression minimally affected the growth of WRI LUAD organoids, thereby excluding possible off-target toxicity. We further confirmed the effect of dnTCF4 overexpression in the xenograft models. Dox treatment decreased the size of xenografts derived from the two WRd organoid lines, along with downregulation of the Wnt target gene *AXIN2* (Figures S7D–SG). Again, the size of WRI LUAD xenografts did not differ between the vehicle and Dox arms, indicating that the effect of Wnt targeting was specific to the WRd LUAD organoids.

To confirm the clinical translatability of Wnt targeting in the treatment of LUAD, we used a porcupine inhibitor (C59). Palmitoylation of Wnt ligands by porcupine is essential for their activation. Consistent with the dependency of WRd LUAD organoids on endogenous Wnt ligands, they grew without exogenous Wnt-3A yet ceased proliferation after supplementation with C59 (Figures 4C and 7A). Exogenous Wnt-3A rescued the growth inhibition by C59 treatment (Figure 7A). C59 treatment downregulated the expression of Wnt target genes, whereas Wnt-3A supplementation abolished this effect (Figure 7B). Notably, all WRd organoid lines, but not WRI organoids, were sensitive to C59 treatment, indicating that C59 specifically targets WRd organoids.

We further determined the *in vivo* effects of C59 using xenografts of LUAD organoids (Figure 7C). C59 treatment produced a significant tumor reduction in two of the three WRd xenograft lines, but not in the two WRI xenograft lines tested, suggesting that its *in vivo* activity was specific to WRd LUAD (Figure 7D). Consistent with this result, C59 significantly decreased *AXIN2* expression in C59-sensitive tumors (Figure 7E). Collectively,

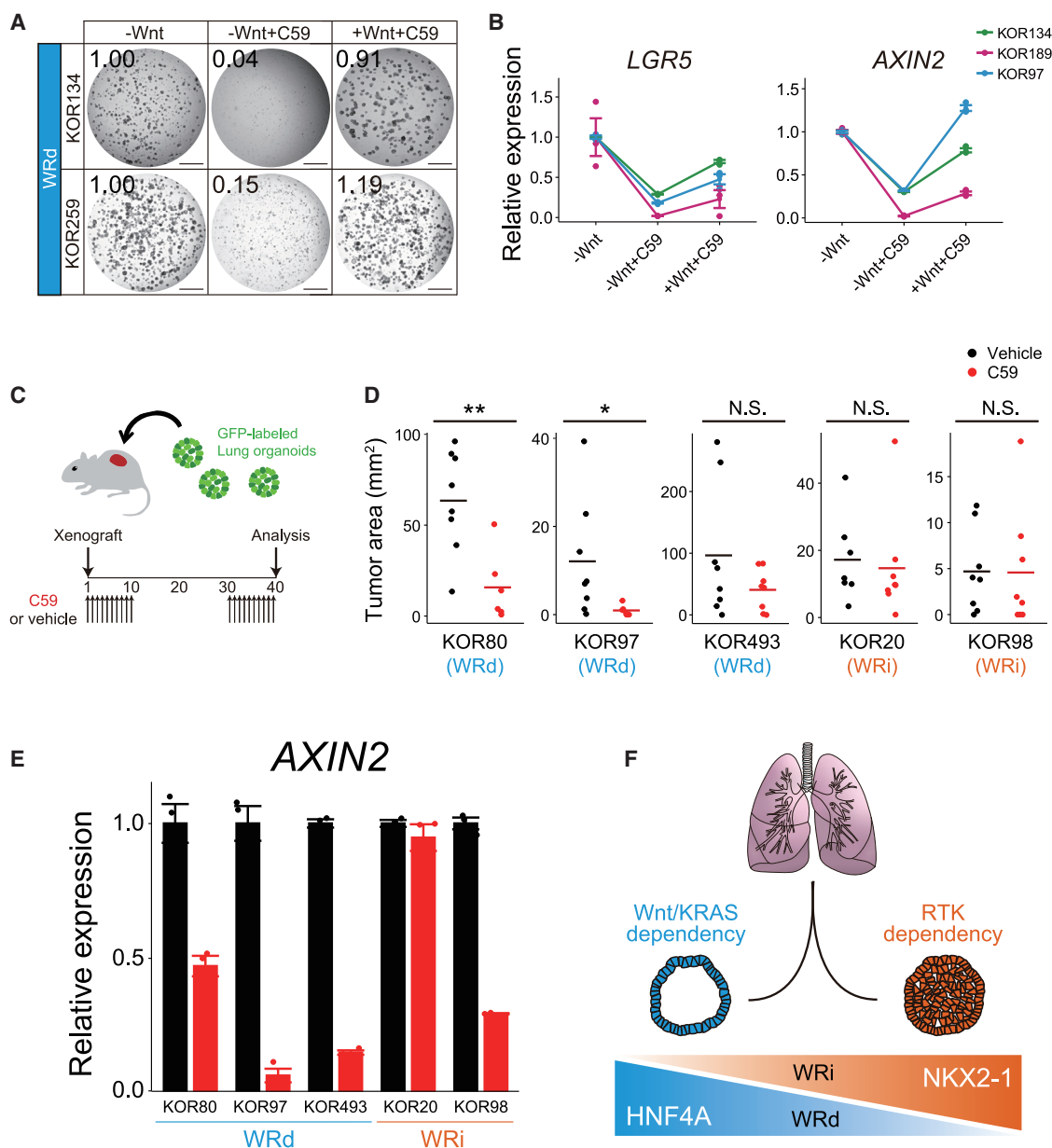


Figure 7. Therapeutic targeting of Wnt in WRd LUAD

(A) Representative images of WRd LUAD organoids cultured without Wnt-3A (left), without Wnt-3A and with C59 (middle), and with Wnt-3A and C59 (right). The mean organoid area relative to that of the -Wnt condition is shown.

(B) The expression of Wnt target genes (*LGR5* and *AXIN2*) in three WRd LUAD organoid lines cultured in the indicated conditions ($n = 3$ per each line for each condition) analyzed by quantitative PCR. mRNA expression (relative to *GAPDH*) levels relative to those of the control condition (-Wnt) are shown.

(C) Subrenal xenotransplantation of green fluorescent protein (GFP)-labeled LUAD organoids and their treatment with C59.

(D) The tumor area of grafts treated with vehicle (black) or C59 (red). Bars indicate the mean area. ** $p < 0.01$, * $p < 0.05$, Wilcoxon's rank-sum test. N.S., not significant.

(E) qPCR analysis of *AXIN2* expression in LC xenografts treated with vehicle (black) or C59 (red). mRNA expression (relative to *GAPDH*) levels relative to those of the control (vehicle) are shown (technical triplicate).

(F) Differential therapeutic strategies for treating NKX2-1-positive and NKX2-1-negative LUAD. NKX2-1-positive LUADs are sensitive to receptor tyrosine kinase (RTK) (EGFR) blockade but resistant to Wnt inhibition. NKX2-1-negative LUADs with gut-like features are enriched for *KRAS* mutations and can be targeted by Wnt inhibition. Scale bar, 1 mm (A). See also Figure S7.

our results reveal bifurcated tumorigenic paths in human LC, each linked with a distinct molecular background (Figure 7F), and that Wnt-targeting therapy may open a therapeutic avenue for patients with LUAD that are refractory to current molecular targeting therapies.

DISCUSSION

Using LC tissues collected using various sampling procedures, we generated an overarching LC organoid library that encompassed the histological and molecular diversity of human LC. In-depth molecular profiling and phenotyping clarified the connections between molecular alterations and LC phenotypes, represented by the phenotypic classification of LUAD into WRi and WRd subgroups and validation of their molecular underpinnings using gene engineering. Epigenetic silencing of *NKX2-1* decreased lung alveolar identity gene signature and induced transcriptional reprogramming-induced gut-like differentiation status and WNT dependency. We further demonstrated that such WNT dependency could be a rational treatment target in *NKX2-1*-negative cases, which account for approximately 20%–30% of LUAD.^{30,31}

Several groups have previously established patient-derived LC organoids.^{9,12,13,15,32} The overall take rate of passageable LC organoids was approximately 20%, which stands on par with the value in our study. The modest establishment efficiency suggests that unknown niche factors may be essential for optimal growth of LC organoids. Overgrowth of contaminating normal alveolar and airway organoids also negatively affects the establishment efficiency. To mitigate this risk while rescuing *TP53*-wild type LC organoids, we enriched LC organoids using an EGF pathway-blocking condition in addition to the conventional Nutlin-3-based method. Attempts to derive organoids from clinical samples collected using non-invasive procedures, such as sputa and CTCs, further enhanced the accessibility to clinical samples and broadened the opportunity for LC organoid derivation. While previous studies suffered from limited cohort sizes and diversity of the organoid biobank, these improvements allowed us to catalog 43 LC organoid lines that clearly represent the major histological subtypes. This LC organoid library, together with comprehensive multiomics data, will provide a valuable resource for the LC research community.

EGFR-RAS pathway mutations in LUAD organoids were not only consistent with the predicted dependency on EIF and response to targeted drugs, but also correlated with dependency on WR. Despite the distinct upstream and downstream regulation of the EGFR and Wnt pathways, *EGFR* and *KRAS* mutations were linked to WR independence and WR dependence in LUAD organoids, respectively. Gene engineering of alveolar organoids consolidated the genotype-phenotype relationship, wherein EGFR-RAS pathway mutations induce WR independence. The phenotypic gap between the WR dependence of *KRAS*-mutated LUAD organoids and WR independence of *KRAS*-engineered alveolar organoids further illuminated the role of lineage reprogramming in the allocation of WR dependency. Multi-omics analysis revealed a characteristic loss of *NKX2-1* and ectopic expression of gut lineage transcription factors in the WRd LUAD organoids. Genetic disruption of *NKX2-1*,

a master regulator of alveolar identity, in *NKX2-1*-expressing WRi LUAD organoids converted them into the WRd type, whereas its overexpression conferred a WRi phenotype to *NKX2-1*-negative WRd organoids, suggesting that lineage plasticity determines the impact of EGFR-RAS pathway mutations on WR dependency. The requirement for *NKX2-1* expression in the induction of the WRi phenotype by EGFR-RAS activation was in agreement with our previous finding that *KRAS* mutation alone did not induce WR independence in intestinal and pancreas organoids.^{27,33} Although the mechanistic linkage between lineage reprogramming and WR dependency remains elusive, our results highlight independent routes to lung carcinogenesis, each characterized by distinct patterns of genetic mutation, WR dependency, and lineage identity.

In contrast with human lung alveolar cells, mouse lung alveolar cells remained dependent on WR in an LC model with mutant *Kras/Trp53*.³⁴ A mouse tumor model with mutant *Braf* also requires Wnt signal activation for tumorigenesis.³⁵ These findings from mouse studies indicate that the Wnt pathway is an attractive drug target for a wide range of LC. However, the high penetrance of WR independence in patient-derived LUAD organoids raises the possibility that patients with LUAD are less likely to benefit from Wnt-targeting therapy. The profiling of LUAD organoids rather suggested that the Wnt targeting approach effectively inhibits the growth of a fraction of LUAD organoids, which are characterized by the absence of *NKX2-1* expression and account for 20%–30% of LUADs.^{30,31} Our findings are consistent with the phenotypes of *NKX2-1*-null, *Braf/Trp53*-mutant mouse lung tumors that showed gastric features and context-dependent Wnt signal activation, although WR dependency was not analyzed in this model.³⁶ High expression of WRd-related genes predicted an unfavorable prognosis in a public LUAD dataset. *NKX2-1*-negative LUAD comprises invasive mucinous adenocarcinoma, a histological variant of LUAD, as well as other histological subtypes, such as acinar and micropapillary adenocarcinomas. Wnt targeting may be a promising treatment option for such *NKX2-1*-negative tumors. From a clinical perspective, *NKX2-1* expression, which is often assessed by immunohistochemistry in clinical pathology, serves as a practical biomarker for predicting the response to Wnt targeting. The efficacy of Wnt inhibitors (porcupine inhibitors) in patients with various cancers is currently under investigation in multiple phase I clinical trials, some of which have confirmed their tolerability in humans.³⁷ Considering the aspects of organoid models that mirror regeneration from tissue stem cells, Wnt inhibition combined with cytotoxic chemotherapy may be effective in blocking the regrowth or recurrence of WRd tumors. Although whether chemotherapy and Wnt-targeting therapy act synergistically requires further investigation, we envision that Wnt inhibitors will cater to unmet needs in the treatment of LUAD, given the limited number of treatment options for *NKX2-1*-negative cases.

In summary, a phenotypic and molecular survey of the human LC organoid library revealed various patterns of growth factor dependency, coupled with genetic abnormalities in human LUAD. A reverse genetics approach using CRISPR engineering and xenografts further demonstrated that such functional liabilities are attractive targets that cannot be distilled from cancer genomics alone. Considering the drawbacks of genomics-focused

precision medicine, our findings highlight the importance of a multidisciplinary framework that harmonizes (epi-)genetic, phenotypic, and engineering approaches to develop strategies to combat human cancer.

Limitations of the study

There are various histological subtypes and endotypes in LUADs, including rare histological subtypes and rare mutational variants. Racial/ethnic background is associated with the different prevalence of those variants. For instance, the prevalence of the EGFR mutation in LUAD is known to be higher in those of Asian descent than in others. As the donors in our LC organoid library are of Japanese ancestry, comparing the molecular and phenotypic characteristics of organoids with multiple racial/ethnic backgrounds will be important in the future. To make our organoid biobanks easily accessible to the community, we are now preparing a cross-sectorial system as a part of the organoid consortium.

Consistent with previous studies,^{9,13,15} the rate of successful LC organoid establishment was approximately 20% in LUAD and LUSC. The modest establishment efficiency was also observed in patient-derived xenograft (PDX) models. Interestingly, the take rate was higher in the organoid model than the PDX model for the establishment of SCLC, whereas PDX enabled better establishment for LUSC lines.^{38,39} Although a side-by-side comparison using the same specimens to draw a conclusion, it is tempting to speculate the presence of unknown tumor-tropic niche factors in the host microenvironment of LUSC xenografts.

STAR★METHODS

Detailed methods are provided in the online version of this paper and include the following:

- **KEY RESOURCES TABLE**
- **RESOURCE AVAILABILITY**
 - Lead contact
 - Materials availability
 - Data and code availability
- **EXPERIMENTAL MODEL AND SUBJECT DETAILS**
 - Organoids
 - Mice
- **METHOD DETAILS**
 - Generation of human lung normal and tumor organoids
 - Xenotransplantation of lung tumor organoids
 - Immunohistochemistry and *in situ* hybridization
 - Drug testing
 - DNA extraction
 - Whole genome sequencing (WGS) analysis and variants call
 - Mutational signature analysis
 - Whole exome sequencing (WES) analysis
 - RNA isolation
 - RNA sequencing of organoids
 - Re-analysis of the TCGA LUAD dataset
 - Quantitative Real-Time PCR
 - Methylation microarray

- ATAC sequence of organoids
- Capillary-based immunoassay
- Gene manipulation of organoids

● QUANTIFICATION AND STATISTICAL ANALYSES

SUPPLEMENTAL INFORMATION

Supplemental information can be found online at <https://doi.org/10.1016/j.celrep.2023.112212>.

ACKNOWLEDGMENTS

We thank Chinatsu Yonekawa for technical assistance. This work was supported by the Japan Agency for Medical Research and Development (AMED) (grant numbers 19cm0106206h0004, 20gm1210001, 21cm0106576h0002, and 22ck0106722h0001), by the JSPS KAKENHI (grant numbers JP19K08610, JP20K17030, JP21H02765, and JP22K08290) and JST Moonshot R&D (grant number JPMJMS2022). A.M., T. Shinozaki, T.F., and H.H. were supported by the Japan Society for the Promotion of Science Research Fellowships for Young Scientists. Genome sequencing analysis was performed in 'SHIROKANE' super-computer of the Human Genome Center, University of Tokyo (<http://supcom.hgc.jp/>), and we acknowledge Ms. Hiroko Tanaka for data management in 'SHIROKANE'.

AUTHOR CONTRIBUTIONS

Conceptualization, T.E., H.Y., and T. Sato; methodology, T.E., J.H., H.Y., and T. Sato; investigation, T.E., J.H., T. Seino, and K.K.; formal analysis, T.E., K. Togasaki, K. Toshimitsu, M.O., T.A.J., and H.N.; resources, T.E., J.H., A.M., K.S., T. Shinozaki, T.F., H.T., S.I., I.K., M.I., K.S., K.F., K.A., T.H., H.A., and H.Y.; writing, T.E., H.A., M.F., and T. Sato; visualization, T.E., J.H., H.H., K.E., and Y.H.; funding acquisition, J.H., H.Y., and T. Sato; project administration, H.Y. and T. Sato.

DECLARATION OF INTERESTS

T.Sato is an inventor on several patents related to organoid culture.

Received: October 21, 2022

Revised: January 6, 2023

Accepted: February 16, 2023

Published: March 6, 2023

REFERENCES

1. Sung, H., Ferlay, J., Siegel, R.L., Laversanne, M., Soerjomataram, I., Jemal, A., and Bray, F. (2021). Global cancer statistics 2020: GLOBOCAN estimates of incidence and mortality worldwide for 36 cancers in 185 countries. *CA Cancer J Clin* 71, 209–249. <https://doi.org/10.3322/caac.21660>.
2. Cancer Genome Atlas Research Network (2014). Comprehensive molecular profiling of lung adenocarcinoma. *Nature* 511, 543–550.
3. Izumi, H., Matsumoto, S., Liu, J., Tanaka, K., Mori, S., Hayashi, K., Kumagai, S., Shibata, Y., Hayashida, T., Watanabe, K., et al. (2021). The CLIP1-LTK fusion is an oncogenic driver in non-small-cell lung cancer. *Nature* 600, 319–323. <https://doi.org/10.1038/s41586-021-04135-5>.
4. Schram, A.M., Chang, M.T., Jonsson, P., and Drilon, A. (2017). Fusions in solid tumours: diagnostic strategies, targeted therapy, and acquired resistance. *Nat. Rev. Clin. Oncol.* 14, 735–748. <https://doi.org/10.1038/nrcl-onc.2017.127>.
5. Frampton, G.M., Ali, S.M., Rosenzweig, M., Chmielecki, J., Lu, X., Bauer, T.M., Akimov, M., Bufile, J.A., Lee, C., Jentz, D., et al. (2015). Activation of MET via diverse exon 14 splicing alterations occurs in multiple tumor types and confers clinical sensitivity to MET inhibitors. *Cancer Discov.* 5, 850–859. <https://doi.org/10.1158/2159-8290.Cd-15-0285>.

6. Drilon, A., Somwar, R., Mangatt, B.P., Edgren, H., Desmeules, P., Ruusu-lehto, A., Smith, R.S., Delasos, L., Vojnic, M., Plodkowski, A.J., et al. (2018). Response to ERBB3-directed targeted therapy in NRG1-rearranged cancers. *Cancer Discov.* 8, 686–695. <https://doi.org/10.1158/2159-8290.Cd-17-1004>.
7. Skoulidis, F., and Heymach, J.V. (2019). Co-occurring genomic alterations in non-small-cell lung cancer biology and therapy. *Nat. Rev. Cancer* 19, 495–509. <https://doi.org/10.1038/s41568-019-0179-8>.
8. Kris, M.G., Johnson, B.E., Berry, L.D., Kwiatkowski, D.J., Iafrate, A.J., Wistuba, I.I., Varella-Garcia, M., Franklin, W.A., Aronson, S.L., Su, P.F., et al. (2014). Using multiplexed assays of oncogenic drivers in lung cancers to select targeted drugs. *JAMA* 311, 1998–2006. <https://doi.org/10.1001/jama.2014.3741>.
9. Dijkstra, K.K., Monkhorst, K., Schipper, L.J., Hartemink, K.J., Smit, E.F., Kaing, S., de Groot, R., Wolkers, M.C., Clevers, H., Cuppen, E., and Voest, E.E. (2020). Challenges in establishing pure lung cancer organoids limit their utility for personalized medicine. *Cell Rep.* 31, 107588. <https://doi.org/10.1016/j.celrep.2020.107588>.
10. Ebisudani, T., Sugimoto, S., Haga, K., Mitsuishi, A., Takai-Todaka, R., Fujii, M., Toshimitsu, K., Hamamoto, J., Sugihara, K., Hishida, T., et al. (2021). Direct derivation of human alveolospheres for SARS-CoV-2 infection modeling and drug screening. *Cell Rep.* 35, 109218. <https://doi.org/10.1016/j.celrep.2021.109218>.
11. Katsura, H., Sontake, V., Tata, A., Kobayashi, Y., Edwards, C.E., Heaton, B.E., Konkimalla, A., Asakura, T., Mikami, Y., Fritch, E.J., et al. (2020). Human lung stem cell-based alveolospheres provide insights into SARS-CoV-2-mediated interferon responses and pneumocyte dysfunction. *Cell Stem Cell* 27, 890–904.e8. <https://doi.org/10.1016/j.stem.2020.10.005>.
12. Kim, M., Mun, H., Sung, C.O., Cho, E.J., Jeon, H.J., Chun, S.M., Jung, D.J., Shin, T.H., Jeong, G.S., Kim, D.K., et al. (2019). Patient-derived lung cancer organoids as in vitro cancer models for therapeutic screening. *Nat. Commun.* 10, 3991. <https://doi.org/10.1038/s41467-019-11867-6>.
13. Sachs, N., Papaspyropoulos, A., Zomer-van Ommen, D.D., Heo, I., Böttinger, L., Klay, D., Weeber, F., Huelsz-Prince, G., Jakobachvili, N., Amantgalim, G.D., et al. (2019). Long-term expanding human airway organoids for disease modeling. *EMBO J.* 38, e100300. <https://doi.org/10.15252/embj.2018100300>.
14. Salahudeen, A.A., Choi, S.S., Rustagi, A., Zhu, J., van Unen, V., de la O, S.M., Flynn, R.A., Margalef-Català, M., Santos, A.J.M., Ju, J., et al. (2020). Progenitor identification and SARS-CoV-2 infection in human distal lung organoids. *Nature* 588, 670–675. <https://doi.org/10.1038/s41586-020-3014-1>.
15. Shi, R., Radulovich, N., Ng, C., Liu, N., Notsuda, H., Cabanero, M., Martins-Filho, S.N., Raghavan, V., Li, Q., Mer, A.S., et al. (2020). Organoid cultures as preclinical models of non-small cell lung cancer. *Clin. Cancer Res.* 26, 1162–1174. <https://doi.org/10.1158/1078-0432.Ccr-19-1376>.
16. Youk, J., Kim, T., Evans, K.V., Jeong, Y.I., Hur, Y., Hong, S.P., Kim, J.H., Yi, K., Kim, S.Y., Na, K.J., et al. (2020). Three-dimensional human alveolar stem cell culture models reveal infection response to SARS-CoV-2. *Cell Stem Cell* 27, 905–919.e10. <https://doi.org/10.1016/j.stem.2020.10.004>.
17. Fujii, M., Shimokawa, M., Date, S., Takano, A., Matano, M., Nanki, K., Ohta, Y., Toshimitsu, K., Nakazato, Y., Kawasaki, K., et al. (2016). A colorectal tumor organoid library demonstrates progressive loss of niche factor requirements during tumorigenesis. *Cell Stem Cell* 18, 827–838. <https://doi.org/10.1016/j.stem.2016.04.003>.
18. Tanaka, F., Yoneda, K., Kondo, N., Hashimoto, M., Takuwa, T., Matsu-moto, S., Okumura, Y., Rahman, S., Tsubota, N., Tsujimura, T., et al. (2009). Circulating tumor cell as a diagnostic marker in primary lung cancer. *Clin. Cancer Res.* 15, 6980–6986.
19. Cancer Genome Atlas Research Network (2012). Comprehensive genomic characterization of squamous cell lung cancers. *Nature* 489, 519–525.
20. George, J., Lim, J.S., Jang, S.J., Cun, Y., Ozretić, L., Kong, G., Leenders, F., Lu, X., Fernández-Cuesta, L., Bosco, G., et al. (2015). Comprehensive genomic profiles of small cell lung cancer. *Nature* 524, 47–53. <https://doi.org/10.1038/nature14664>.
21. George, J., Walter, V., Peifer, M., Alexandrov, L.B., Seidel, D., Leenders, F., Maas, L., Müller, C., Dahmen, I., Delhomme, T.M., et al. (2018). Integrative genomic profiling of large-cell neuroendocrine carcinomas reveals distinct subtypes of high-grade neuroendocrine lung tumors. *Nat. Commun.* 9, 1048. <https://doi.org/10.1038/s41467-018-03099-x>.
22. Alexandrov, L.B., Kim, J., Haradhvala, N.J., Huang, M.N., Tian Ng, A.W., Wu, Y., Boot, A., Covington, K.R., Gordenin, D.A., Bergstrom, E.N., et al. (2020). The repertoire of mutational signatures in human cancer. *Nature* 578, 94–101. <https://doi.org/10.1038/s41586-020-1943-3>.
23. Nanki, K., Fujii, M., Shimokawa, M., Matano, M., Nishikori, S., Date, S., Takano, A., Toshimitsu, K., Ohta, Y., Takahashi, S., et al. (2020). Somatic inflammatory gene mutations in human ulcerative colitis epithelium. *Nature* 577, 254–259. <https://doi.org/10.1038/s41586-019-1844-5>.
24. de Bruin, E.C., McGranahan, N., Mitter, R., Salm, M., Wedge, D.C., Yates, L., Jamal-Hanjani, M., Shafi, S., Murugaes, N., Rowan, A.J., et al. (2014). Spatial and temporal diversity in genomic instability processes defines lung cancer evolution. *Science* 346, 251–256. <https://doi.org/10.1126/science.1253462>.
25. Katsura, H., Kobayashi, Y., Tata, P.R., and Hogan, B.L.M. (2019). IL-1 and TNF α contribute to the inflammatory niche to enhance alveolar regeneration. *Stem Cell Reports* 12, 657–666. <https://doi.org/10.1016/j.stemcr.2019.02.013>.
26. Kawasaki, K., Toshimitsu, K., Matano, M., Fujita, M., Fujii, M., Togasaki, K., Ebisudani, T., Shimokawa, M., Takano, A., Takahashi, S., et al. (2020). An organoid biobank of neuroendocrine neoplasms enables genotype-phenotype mapping. *Cell* 183, 1420–1435.e21. <https://doi.org/10.1016/j.cell.2020.10.023>.
27. Seino, T., Kawasaki, S., Shimokawa, M., Tamagawa, H., Toshimitsu, K., Fujii, M., Ohta, Y., Matano, M., Nanki, K., Kawasaki, K., et al. (2018). Human pancreatic tumor organoids reveal loss of stem cell niche factor dependence during disease progression. *Cell Stem Cell* 22, 454–467.e6. <https://doi.org/10.1016/j.stem.2017.12.009>.
28. Nanki, K., Toshimitsu, K., Takano, A., Fujii, M., Shimokawa, M., Ohta, Y., Matano, M., Seino, T., Nishikori, S., Ishikawa, K., et al. (2018). Divergent routes toward Wnt and R-spondin niche independency during human gastric carcinogenesis. *Cell* 174, 856–869.e17. <https://doi.org/10.1016/j.cell.2018.07.027>.
29. van de Wetering, M., Sancho, E., Verweij, C., de Lau, W., Oving, I., Hurlstone, A., van der Horn, K., Battle, E., Coudreuse, D., Haramis, A.P., et al. (2002). The beta-catenin/TCF-4 complex imposes a crypt progenitor phenotype on colorectal cancer cells. *Cell* 111, 241–250.
30. Sun, J.M., Han, J., Ahn, J.S., Park, K., and Ahn, M.J. (2011). Significance of thymidylate synthase and thyroid transcription factor 1 expression in patients with nonsquamous non-small cell lung cancer treated with pemetrexed-based chemotherapy. *J. Thorac. Oncol.* 6, 1392–1399. <https://doi.org/10.1097/JTO.0b013e3182208ea8>.
31. Frost, N., Zhamurashvili, T., von Laffert, M., Klauschen, F., Ruwwe-Glößenkamp, C., Raspe, M., Brunn, M., Ochsenreither, S., Temmesfeld-Wollbrück, B., Suttrop, N., et al. (2020). Pemetrexed-based chemotherapy is inferior to pemetrexed-free regimens in thyroid transcription factor 1 (TTF-1)-Negative, EGFR/ALK-negative lung adenocarcinoma: a propensity score matched pairs analysis. *Clin. Lung Cancer* 21, e607–e621. <https://doi.org/10.1016/j.clcl.2020.05.014>.
32. Kim, S.Y., Kim, S.M., Lim, S., Lee, J.Y., Choi, S.J., Yang, S.D., Yun, M.R., Kim, C.G., Gu, S.R., Park, C., et al. (2021). Modeling clinical responses to targeted therapies by patient-derived organoids of advanced lung adenocarcinoma. *Clin. Cancer Res.* 27, 4397–4409. <https://doi.org/10.1158/1078-0432.Ccr-20-5026>.
33. Matano, M., Date, S., Shimokawa, M., Takano, A., Fujii, M., Ohta, Y., Watanabe, T., Kanai, T., and Sato, T. (2015). Modeling colorectal cancer using CRISPR-Cas9-mediated engineering of human intestinal organoids. *Nat. Med* 21, 256–262. <https://doi.org/10.1038/nm.3802>.

34. Tammela, T., Sanchez-Rivera, F.J., Cetinbas, N.M., Wu, K., Joshi, N.S., Helenius, K., Park, Y., Azimi, R., Kerper, N.R., Wesselhoeft, R.A., et al. (2017). A Wnt-producing niche drives proliferative potential and progression in lung adenocarcinoma. *Nature* 545, 355–359. <https://doi.org/10.1038/nature22334>.
35. Juan, J., Muraguchi, T., Iezza, G., Sears, R.C., and McMahon, M. (2014). Diminished WNT → β -catenin → c-MYC signaling is a barrier for malignant progression of BRAFV600E-induced lung tumors. *Genes Dev* 28, 561–575. <https://doi.org/10.1101/gad.233627.113>.
36. Zewdu, R., Mehrabad, E.M., Ingram, K., Fang, P., Gillis, K.L., Camolotto, S.A., Orstad, G., Jones, A., Mendoza, M.C., Spike, B.T., and Snyder, E.L. (2021). An NKX2-1/ERK/WNT feedback loop modulates gastric identity and response to targeted therapy in lung adenocarcinoma. *Elife* 10, e66788. <https://doi.org/10.7554/eLife.66788>.
37. Shah, K., Panchal, S., and Patel, B. (2021). Porcupine inhibitors: novel and emerging anti-cancer therapeutics targeting the Wnt signaling pathway. *Pharmacol. Res.* 167, 105532. <https://doi.org/10.1016/j.phrs.2021.105532>.
38. Caesar, R., Egger, J.V., Chavan, S., Socci, N.D., Jones, C.B., Kombak, F.E., Asher, M., Roehrl, M.H., Shah, N.S., Allaj, V., et al. (2022). Genomic and transcriptomic analysis of a library of small cell lung cancer patient-derived xenografts. *Nat. Commun.* 13, 2144. <https://doi.org/10.1038/s41467-022-29794-4>.
39. Mirhadi, S., Tam, S., Li, Q., Moghal, N., Pham, N.A., Tong, J., Golbourn, B.J., Krieger, J.R., Taylor, P., Li, M., et al. (2022). Integrative analysis of non-small cell lung cancer patient-derived xenografts identifies distinct proteotypes associated with patient outcomes. *Nat. Commun.* 13, 1811. <https://doi.org/10.1038/s41467-022-29444-9>.
40. Randolph, L.N., Bao, X., Zhou, C., and Lian, X. (2017). An all-in-one, Tet-On 3G inducible PiggyBac system for human pluripotent stem cells and derivatives. *Sci. Rep.* 7, 1549. <https://doi.org/10.1038/s41598-017-01684-6>.
41. Cong, L., Ran, F.A., Cox, D., Lin, S., Barretto, R., Habib, N., Hsu, P.D., Wu, X., Jiang, W., Marraffini, L.A., and Zhang, F. (2013). Multiplex genome engineering using CRISPR/Cas systems. *Science* 339, 819–823. <https://doi.org/10.1126/science.1231143>.
42. Martin, M. (2011). Cutadapt removes adapter sequences from high-throughput sequencing reads. *EMBnet (J)*, 10–12.
43. Dobin, A., Davis, C.A., Schlesinger, F., Drenkow, J., Zaleski, C., Jha, S., Batut, P., Chaisson, M., and Gingeras, T.R. (2013). STAR: ultrafast universal RNA-seq aligner. *Bioinformatics* 29, 15–21. <https://doi.org/10.1093/bioinformatics/bts635>.
44. Li, B., and Dewey, C.N. (2011). RSEM: accurate transcript quantification from RNA-Seq data with or without a reference genome. *BMC Bioinformatics* 12, 323. <https://doi.org/10.1186/1471-2105-12-323>.
45. Love, M.I., Huber, W., and Anders, S. (2014). Moderated estimation of fold change and dispersion for RNA-seq data with DESeq2. *Genome Biol* 15, 550. <https://doi.org/10.1186/s13059-014-0550-8>.
46. Pidsley, R., Y Wong, C.C., Volta, M., Lunnon, K., Mill, J., and Schalkwyk, L.C. (2013). A data-driven approach to preprocessing Illumina 450K methylation array data. *BMC Genomics* 14, 293. <https://doi.org/10.1186/1471-2164-14-293>.
47. Li, H., and Durbin, R. (2009). Fast and accurate short read alignment with Burrows-Wheeler transform. *Bioinformatics* 25, 1754–1760. <https://doi.org/10.1093/bioinformatics/btp324>.
48. Li, H., Handsaker, B., Wysoker, A., Fennell, T., Ruan, J., Homer, N., Marth, G., Abecasis, G., and Durbin, R.; 1000 Genome Project Data Processing Subgroup (2009). The sequence alignment/map format and SAMtools. *Bioinformatics* 25, 2078–2079. <https://doi.org/10.1093/bioinformatics/btp352>.
49. Brinkman, E.K., Chen, T., Amendola, M., and van Steensel, B. (2014). Easy quantitative assessment of genome editing by sequence trace decomposition. *Nucleic Acids Res* 42, e168. <https://doi.org/10.1093/nar/gku936>.
50. Wang, K., Li, M., and Hakonarson, H. (2010). ANNOVAR: functional annotation of genetic variants from high-throughput sequencing data. *Nucleic Acids Res* 38, e164. <https://doi.org/10.1093/nar/gkq603>.
51. Cingolani, P., Platts, A., Wang, L.L., Coon, M., Nguyen, T., Wang, L., Land, S.J., Lu, X., and Ruden, D.M. (2012). A program for annotating and predicting the effects of single nucleotide polymorphisms, SnpEff: SNPs in the genome of *Drosophila melanogaster* strain w1118; iso-2; iso-3. *Fly* 6, 80–92.
52. Priestley, P., Baber, J., Lolkema, M.P., Steeghs, N., de Bruijn, E., Shale, C., Duyvesteyn, K., Haidari, S., van Hoeck, A., Onstenk, W., et al. (2019). Pan-cancer whole-genome analyses of metastatic solid tumours. *Nature* 575, 210–216. <https://doi.org/10.1038/s41586-019-1689-y>.
53. Cameron, D.L., Baber, J., Shale, C., Valle-Inclan, J.E., Besselink, N., van Hoeck, A., Janssen, R., Cuppen, E., Priestley, P., and Papenfuss, A.T. (2021). GRIDSS2: comprehensive characterisation of somatic structural variation using single breakend variants and structural variant phasing. *Genome Biol.* 22, 1–25.
54. Shale, C., Cameron, D.L., Baber, J., Wong, M., Cowley, M.J., Papenfuss, A.T., Cuppen, E., and Priestley, P. (2022). Unscrambling cancer genomes via integrated analysis of structural variation and copy number. *Cell Genom.* 2, 100112.
55. Islam, S.A., Wu, Y., Díaz-Gay, M., Bergstrom, E.N., He, Y., Barnes, M., Vella, M., Wang, J., Teague, J.W., and Clapham, P. (2021). Uncovering novel mutational signatures by de novo extraction with SigProfilerExtractor. Preprint at bioRxiv.
56. Bergstrom, E.N., Huang, M.N., Mahto, U., Barnes, M., Stratton, M.R., Rozen, S.G., and Alexandrov, L.B. (2019). SigProfilerMatrixGenerator: a tool for visualizing and exploring patterns of small mutational events. *BMC Genom.* 20, 1–12.
57. Johnson, T.A., Maekawa, S., Fujita, M., An, J., Ju, Y.S., Maejima, K., Kanazashi, Y., Jikuya, R., Okawa, Y., Sasagawa, S., et al. (2023). Genomic features of renal cell carcinoma developed during end-stage renal disease and dialysis. *Hum. Mol. Genet.* 32, 290–303. <https://doi.org/10.1093/hmg/ddac180>.
58. Langmead, B., and Salzberg, S.L. (2012). Fast gapped-read alignment with Bowtie 2. *Nat. Methods* 9, 357–359. <https://doi.org/10.1038/nmeth.1923>.
59. Zhang, Y., Liu, T., Meyer, C.A., Eeckhoutte, J., Johnson, D.S., Bernstein, B.E., Nussbaum, C., Myers, R.M., Brown, M., Li, W., and Liu, X.S. (2008). Model-based analysis of ChIP-seq (MACS). *Genome Biol* 9, R137. <https://doi.org/10.1186/gb-2008-9-9-r137>.
60. Heinz, S., Benner, C., Spann, N., Bertolino, E., Lin, Y.C., Laslo, P., Cheng, J.X., Murre, C., Singh, H., and Glass, C.K. (2010). Simple combinations of lineage-determining transcription factors prime cis-regulatory elements required for macrophage and B cell identities. *Mol. Cell* 38, 576–589. <https://doi.org/10.1016/j.molcel.2010.05.004>.
61. Ramírez, F., Dündar, F., Diehl, S., Grüning, B.A., and Manke, T. (2014). deepTools: a flexible platform for exploring deep-sequencing data. *Nucleic Acids Res* 42, W187–W191. <https://doi.org/10.1093/nar/gku365>.
62. Schep, A.N., Wu, B., Buenrostro, J.D., and Greenleaf, W.J. (2017). chromVAR: inferring transcription-factor-associated accessibility from single-cell epigenomic data. *Nat. Methods* 14, 975–978. <https://doi.org/10.1038/nmeth.4401>.
63. Fujii, M., Matano, M., Toshimitsu, K., Takano, A., Mikami, Y., Nishikori, S., Sugimoto, S., and Sato, T. (2018). Human intestinal organoids maintain self-renewal capacity and cellular diversity in niche-inspired culture condition. *Cell Stem Cell* 23, 787–793.e6. <https://doi.org/10.1016/j.stem.2018.11.016>.

64. Mihara, E., Hirai, H., Yamamoto, H., Tamura-Kawakami, K., Matano, M., Kikuchi, A., Sato, T., and Takagi, J. (2016). Active and water-soluble form of lipidated Wnt protein is maintained by a serum glycoprotein afamin/ α -albumin. *Elife* 5. <https://doi.org/10.7554/eLife.11621>.
65. Drost, J., Karthaus, W.R., Gao, D., Driehuis, E., Sawyers, C.L., Chen, Y., and Clevers, H. (2016). Organoid culture systems for prostate epithelial and cancer tissue. *Nat. Protoc.* 11, 347–358. <https://doi.org/10.1038/nprot.2016.006>.
66. Fujii, M., Matano, M., Nanki, K., and Sato, T. (2015). Efficient genetic engineering of human intestinal organoids using electroporation. *Nat. Protoc.* 10, 1474–1485. <https://doi.org/10.1038/nprot.2015.088>.
67. Cameron, D.L., Baber, J., Shale, C., Papenfuss, A.T., Valle-Inclan, J.E., Besselink, N., Cuppen, E., and Priestley, P. (2019). GRIDSS, PURPLE, LINX: unscrambling the tumor genome via integrated analysis of structural variation and copy number. Preprint at bioRxiv, 781013. <https://doi.org/10.1101/781013>.
68. Higasa, K., Miyake, N., Yoshimura, J., Okamura, K., Niihori, T., Saito, H., Doi, K., Shimizu, M., Nakabayashi, K., Aoki, Y., et al. (2016). Human genetic variation database, a reference database of genetic variations in the Japanese population. *J. Hum. Genet.* 61, 547–553. <https://doi.org/10.1038/jhg.2016.12>.
69. Korotkevich, G., Sukhov, V., and Sergushichev, A. (2019). Fast gene set enrichment analysis. Preprint at bioRxiv, 060012. <https://doi.org/10.1101/060012>.
70. Guo, M., Tomoshige, K., Meister, M., Muley, T., Fukazawa, T., Tsuchiya, T., Kams, R., Warth, A., Fink-Baldauf, I.M., Nagayasu, T., et al. (2017). Gene signature driving invasive mucinous adenocarcinoma of the lung. *EMBO Mol. Med.* 9, 462–481. <https://doi.org/10.15252/emmm.201606711>.
71. Liu, J., Lichtenberg, T., Hoadley, K.A., Poisson, L.M., Lazar, A.J., Cherniack, A.D., Kovatich, A.J., Benz, C.C., Levine, D.A., Lee, A.V., et al. (2018). An integrated TCGA pan-cancer clinical data resource to drive high-quality survival outcome analytics. *Cell* 173, 400–416.e11. <https://doi.org/10.1016/j.cell.2018.02.052>.
72. Foroutan, M., Bhuva, D.D., Lyu, R., Horan, K., Cursons, J., and Davis, M.J. (2018). Single sample scoring of molecular phenotypes. *BMC Bioinformatics* 19, 404. <https://doi.org/10.1186/s12859-018-2435-4>.
73. Corces, M.R., Trevino, A.E., Hamilton, E.G., Greenside, P.G., Sinnott-Armstrong, N.A., Vesuna, S., Satpathy, A.T., Rubin, A.J., Montine, K.S., Wu, B., et al. (2017). An improved ATAC-seq protocol reduces background and enables interrogation of frozen tissues. *Nat. Methods* 14, 959–962. <https://doi.org/10.1038/nmeth.4396>.
74. Buenrostro, J.D., Giresi, P.G., Zaba, L.C., Chang, H.Y., and Greenleaf, W.J. (2013). Transposition of native chromatin for fast and sensitive epigenomic profiling of open chromatin, DNA-binding proteins and nucleosome position. *Nat. Methods* 10, 1213–1218. <https://doi.org/10.1038/nmeth.2688>.
75. Weirauch, M.T., Yang, A., Albu, M., Cote, A.G., Montenegro-Montero, A., Drewe, P., Najafabadi, H.S., Lambert, S.A., Mann, I., Cook, K., et al. (2014). Determination and inference of eukaryotic transcription factor sequence specificity. *Cell* 158, 1431–1443. <https://doi.org/10.1016/j.cell.2014.08.009>.

STAR★METHODS

KEY RESOURCES TABLE

REAGENT or RESOURCE	SOURCE	IDENTIFIER
Antibodies		
Rabbit polyclonal anti-p44/42 MAPK (Erk1/2)	Cell Signaling Technology	Cat#9102, RRID: AB_330744
Rabbit monoclonal anti-phospho-p44/42 MAPK (Erk1/2) (Thr202/Tyr204) (D13.14.4E)	Cell Signaling Technology	Cat#4370, RRID: AB_2315112
Rabbit monoclonal anti-TTF1 (EP1584Y)	Abcam	Cat#ab76013, RRID: AB_1310784
Mouse monoclonal anti- β -actin	Sigma-Aldrich	Cat#A1978, RRID: AB_476692
Rabbit polyclonal anti-TP53	Cell Signaling Technology	Cat#9282, RRID: AB_331476
Alexa Fluor 647-Mouse monoclonal anti-human CD326 (EpCAM) (9C4)	BioLegend	Cat#324212, RRID: AB_756086
Mouse monoclonal anti-HT2-280	Terrace Biotech	Cat#TB-27AHT2-280, RRID: AB_2832931
Mouse monoclonal anti-NKX2-1 (8G7G3/1)	Dako	Cat#M3575, RRID: AB_2877699
Mouse monoclonal anti-KRT7 (OV-TL12/30)	Dako	Cat#M7018, RRID: AB_2134589
Mouse monoclonal anti-p40 (BC28)	Nichirei Biosciences	Cat#418171
Rabbit polyclonal anti-KRT5	Spring Bioscience	Cat#E13820, RRID: AB_1661300
Rabbit polyclonal anti-Synaptophysin	Dako	Cat#A0010, RRID: AB_2315411
Rabbit polyclonal anti-Chromogranin A	Dako	Cat#A0430, RRID: AB_2847855
Mouse monoclonal anti-CD56 (123C3)	Dako	Cat#M7304, RRID: AB_2750583
Mouse monoclonal anti- β -catenin (14/Beta-Catenin)	BD Biosciences	Cat#610153, RRID: AB_397555
Mouse monoclonal anti-HNF4 α (C11F12)	Cell Signaling Technology	Cat#3113S, RRID: AB_2295208
Rabbit monoclonal anti-TCF4/TCF7L2 (C48H11)	Cell Signaling Technology	Cat#2569S, RRID: AB_2199816
Donkey polyclonal anti-mouse IgG (H + L), Alexa Fluor 488	Thermo Fisher Scientific	Cat#A-21202, RRID: AB_141607
Donkey polyclonal anti-mouse IgG (H + L), Alexa Fluor 647	Thermo Fisher Scientific	Cat#A-31571, RRID: AB_162542
Donkey polyclonal anti-rabbit IgG (H + L), Alexa Fluor 568	Thermo Fisher Scientific	Cat#A10042, RRID: AB_2534017
Biological samples		
Human lung tissue samples	This paper	N/A
Human blood samples for sequence analyses	This paper	N/A
Chemicals, peptides, and recombinant proteins		
Advanced DMEM/F12	Thermo Fisher Scientific	Cat#12634010
HEPES	Thermo Fisher Scientific	Cat#15630080
Penicillin-Streptomycin	Thermo Fisher Scientific	Cat#15140122
GlutaMAX Supplement	Thermo Fisher Scientific	Cat#35050061
Matrigel	Corning	Cat#356231
B-27 Supplement	Thermo Fisher Scientific	Cat#17504044
N-Acetyl-L-cysteine	Sigma-Aldrich	Cat#A9165
[Leu ¹⁵]-Gastrin I human	Sigma-Aldrich	Cat#G9145
Afamin-Wnt-3A serum-free conditioned medium	Mihara et al., 2016 ⁴¹	N/A
Recombinant mouse EGF	Thermo Fisher Scientific	Cat#PMG8043
Recombinant human IGF-1	BioLegend	Cat#590904

(Continued on next page)

Continued

REAGENT or RESOURCE	SOURCE	IDENTIFIER
Recombinant human FGF-basic	Peprtech	Cat#100-18B
Recombinant human neuregulin-1 (Heregulin β -1)	Peprtech	Cat#100-03
Wnt-C59	ShangHai Biochempartner	Cat#1243243-89-1
Recombinant mouse Noggin	Peprtech	Cat#250-38
Recombinant human R-spondin1	R&D	Cat#4645-RS
A83-01	Tocris	Cat#2939
Y-27632	FUJIFILM Wako Pure Chemical	Cat#253-00513
Cell Recovery Solution	Corning	Cat#354253
Liberase TH Research Grade	Roche	Cat#05401151001
TrypLE Express	Thermo Fisher Scientific	Cat#12605010
Suptazyme	KYOKUTO PHARMACEUTICAL INDUSTRIAL CO., LTD	Cat#15200
Red Blood Cell Lysis Buffer	Roche	Cat#11814389001
RosetteSep™ CTC Enrichment Cocktail Containing Anti-CD36	Stem Cell Technologies	Cat#15127
Ficoll-Paque PLUS	GE	Cat# 17144002
Hoechst 33342	Thermo Fisher Scientific	Cat#H3570
Doxycycline	Sigma-Aldrich	Cat#D9891
Puromycin	Thermo Fisher Scientific	Cat#A1113803
Blasticidin	Thermo Fisher Scientific	Cat#A11139-03
(\pm)-Nutlin-3	Cayman Chemical	Cat#548472-68-0
EGFR/ErbB-2/ErbB4 inhibitor	Merck Millipore	Cat#324840
Sotorasib	Selleck	Cat#S8830
Alectinib	Selleck	Cat#S2762
Dabrafenb	Chemscene	Cat#CS-0692
ProLong Diamond Antifade Mountant	Thermo Fisher Scientific	Cat#P36961
Power Block Universal Blocking Reagent	BioGenex	Cat#HK083-50K
BTXpress Solution	BTX	Cat#45-0805
Opti-MEM I Reduced Serum Medium	Thermo Fisher Scientific	Cat#31985062
RNase cocktail enzyme mix	Thermo Fisher Scientific	Cat#AM2286
Deoxyribonuclease 1	Worthington Biochemical Corporation	Cat#3.1.21.1
NEBNext High-Fidelity 2X PCR Master Mix	New England BioLabs	Cat#M0541
Critical commercial assays		
RNAscope 2.5 HD Reagent Kit	Advanced Cell Diagnostics	Cat#322350
QIAamp DNA Blood Mini Kit	QIAGEN	Cat#51106
RNeasy Plus Mini Kit	QIAGEN	Cat#74134
High-Capacity RNA-to-cDNA Kit	Thermo Fisher Scientific	Cat#4387406
KAPA SYBR® FAST qPCR Kits	KAPABIOSYSTEMS	Cat#KK4605
TruSeq RNA Library Prep Kit v2	Illumina	Cat#RS-122-2001
SureSelect XT Human All exon V6	Agilent	Cat#5190-8864
Infinium MethylationEPIC BeadChip Kit	Illumina	Cat#WG-317-1001
Wes 12–230 kDa Master Kit	ProteinSimple	N/A
12-230 kDa Wes Separation Module, capillary cartridges	ProteinSimple	Cat#SM-W004
Anti-Mouse Detection Module for Jess, Wes, Peggy Sue or Sally Sue	ProteinSimple	Cat#DM002
Anti-Rabbit Detection Module for Jess, Wes, Peggy Sue or Sally Sue	ProteinSimple	Cat#DM001

(Continued on next page)

Continued

REAGENT or RESOURCE	SOURCE	IDENTIFIER
Plasmid Plus Maxi Kit	QIAGEN	Cat#12965
CellTiter-GLO 3D Cell Viability Assay	Promega	Cat#G9681
iPGell	GenoStaff	Cat#PG20-1
Deposited data		
WGS and WES data of LC organoids	This paper	Data will be deposited.
RNA-seq data of genetically engineered and LC organoids	This paper	Data will be deposited.
ENCODE hg 38 blacklist	The ENCODE Project Consortium, 2012	https://www.encodeproject.org/annotations/ENCSR636HFF/
dbSNP	NIH	https://www.ncbi.nlm.nih.gov/snp/
Human Genetic Variation Database	HGVD	https://www.hgvd.genome.med.kyoto-u.ac.jp/
Experimental models: Cell lines		
Human: normal airway and alveolar organoids: see Table S1	This paper	N/A
Human: lung cancer organoids: see Table S1	This paper	N/A
Experimental models: Organisms/strains		
Mouse: BALB/c- <i>nu/nu</i>	Oriental Yeast Co., Ltd	N/A
Mouse: <i>NOD/Shi-scid, IL-2Rg^{null}</i>	In-Vivo Science	N/A
Oligonucleotides		
TP53 - gRNA	Matano et al., 2015 ³³	Table S7
CDKN2A - gRNA	Seino et al., 2018 ²⁷	Table S7
NKX2-1 - gRNA	This paper	Table S7
GAPDH - qPCR forward primer	This paper	Table S7
GAPDH - qPCR reverse primer	This paper	Table S7
AXIN2 - qPCR forward primer	This paper	Table S7
AXIN2 - qPCR reverse primer	This paper	Table S7
LGR5 - qPCR forward primer	This paper	Table S7
LGR5 - qPCR reverse primer	This paper	Table S7
RNAscope Probe Hs-AXIN2	Advanced Cell Diagnostics	Cat#400241
RNAscope Positive Control Probe Hs-PPIB	Advanced Cell Diagnostics	Cat#313901
RNAscope Negative Control Probe DapB	Advanced Cell Diagnostics	Cat#310043
Recombinant DNA		
dnTCF4 donor vector	van de Wetering et al., 2002 ²⁹	N/A
PB-CMV-MCS-EF1a-GFP-Puro vector	System Biosciences	Cat#PB513B-1
Super PiggyBac Transposase Expression Vector	System Biosciences	Cat#PB210PA-1
XLone-GFP	Randolph et al., 2017 ⁴⁰	Addgene Plasmid #96930
pX330-U6-Chimeric_BB-CBh-hSpCas9	Cong et al., 2013 ⁴¹	Addgene Plasmid#42230
pLVSIIN-EF1a-IRES-ZsGreen1	TaKaRa	Cat#6192
lentiCRISPR v2-Blast	N/A	Addgene Plasmid#83480
Software and algorithms		
R v. 4.0.3	Comprehensive R Archive Network	https://cran.r-project.org/
cutadapt v. 1.18	Martin, 2011 ⁴²	https://cutadapt.readthedocs.io/en/stable/installation.html
STAR v. 2.6.1b	Dobin et al., 2013 ⁴³	https://github.com/alexdobin/STAR
RSEM (version 1.3.3)	Li et al., 2011 ⁴⁴	https://github.com/deweylab/RSEM

(Continued on next page)

Continued

REAGENT or RESOURCE	SOURCE	IDENTIFIER
R Bioconductor package DESeq2	Bioconductor, Love et al., 2014 ⁴⁵	http://bioconductor.org/packages/release/bioc/html/DESeq2.html
Applied Biosystems 7500 Fast	Thermo Fisher Scientific	N/A
R Bioconductor package watermelon	Pidsley et al., 2013 ⁴⁶	https://bioconductor.org/packages/release/bioc/html/watermelon.html
Rtsne v. 0.15	Github	https://github.com/jkrijthe/Rtsne
Burrows-Wheeler Aligner (BWA)	Li and Durbin, 2009 ⁴⁷	http://bio-bwa.sourceforge.net/
Genome Analysis Toolkit (GATK) v. 4.1.2.0	Broad Institute	https://gatk.broadinstitute.org
Samtools	Li et al., 2009 ⁴⁸	http://www.htslib.org/
Compass for SW	ProteinSimple	http://www.proteinsimple.com/compass/downloads/
TIDE web tool	Netherlands Cancer Institute, Brinkman et al., 2014 ⁴⁹	https://tide.deskgen.com/
Biobambam	Wellcome Sanger institute	https://www.sanger.ac.uk/tool/biobambam/
ANNOVAR	Wang et al., 2010 ⁵⁰	http://wannovar.wglab.org/index.php
snEff	Cingolani et al., 2012 ⁵¹	http://pcingola.github.io/SnpEff/
ALFA	National Center for Biotechnology Information	https://ftp.ncbi.nih.gov/snp/population_frequency/latest_release/freqs.vcf.gz
SAGE	Priestley et al., 2019 ⁵²	https://github.com/hartwigmedical/hmftools/releases/tag/sage-v2.8
GRIDSS	Cameron et al., 2021 ⁵³	https://github.com/PapenfussLab/gridss
GRIPSS	Priestley et al., 2019 ⁵²	https://github.com/hartwigmedical/hmftools/tree/master/gripss
AMBER	Priestley et al., 2019 ⁵²	https://github.com/hartwigmedical/hmftools/tree/master/amber
COBALT	Priestley et al., 2019 ⁵²	https://github.com/hartwigmedical/hmftools/tree/master/cobalt
PURPLE	Priestley et al., 2019 ⁵²	https://github.com/hartwigmedical/hmftools/tree/master/purple
Linx	Shale et al., 2022 ⁵⁴	https://github.com/hartwigmedical/hmftools/tree/master/linx
SigProfilerExtractor	Islam et al., 2021 ⁵⁵	https://github.com/AlexandrovLab/SigProfilerExtractor
SigProfilerMatrixGenerator	Bergstrom et al., 2019 ⁵⁶	https://github.com/AlexandrovLab/SigProfilerMatrixGenerator
Tumor-GRaPPLer WGS analysis workflow	Johnson et al., 2023 ⁵⁷	https://github.com/toddajohnson/tumor-grappler
Bowtie2	Langmead and Salzberg, 2012 ⁵⁸	https://sourceforge.net/projects/bowtie-bio/files/bowtie2/
MACS2	Pidsley et al., 2013 ⁴⁶ ; Zhang et al., 2008 ⁵⁹	https://github.com/mac3-project/MACS
HOMER	Heinz et al., 2010 ⁶⁰ ; Pidsley et al., 2013 ⁴⁶	http://homer.ucsd.edu/homer/
Deeptools	Ramírez et al., 2014 ⁶¹	https://github.com/deeptools/deepTools
R Bioconductor package chromVAR	Schep et al., 2017 ⁶²	https://github.com/GreenleafLab/chromVAR
LAS X	Leica Microsystems	https://www.leica-microsystems.com/products/microscope-software/
LuminaVision	Mitani	https://www.mitani-visual.jp/download/catalogs/
BZ-X analyzer	Keyence	N/A

RESOURCE AVAILABILITY

Lead contact

Further information and requests for resources and reagents should be directed to and will be fulfilled by the Lead Contact, Dr. Toshiro Sato (t.sato@keio.jp).

Materials availability

All unique/stable reagents generated in this study are available from the [lead contact](#) with a completed Materials Transfer Agreement.

Data and code availability

- WGS, WES, RNA-seq, methylation microarray, and ATAC-seq data are deposited in the Japanese Genotype-phenotype Archive under the accession number JGAS000557.
- This paper does not report original code.
- Any additional information required to reanalyze the data reported in this paper is available from the [lead contact](#) upon request.

EXPERIMENTAL MODEL AND SUBJECT DETAILS

Organoids

Human normal lung samples were obtained from patients with written informed consent after an approval by the ethical committee of Keio University School of Medicine. Detailed clinical information is provided in [Table S1](#). The method for the establishment of human normal and tumor organoids is described in the later section.

Mice

All animal procedures were approved by the Keio University School of Medicine Animal Care Committee. Female *NOD/Shi-scid, IL-2R γ ^{null}* (NOG) mice (7–12 weeks old) were obtained from the In-Vivo Science and female BALB/c-*nu/nu* mice (7–12 weeks old) were obtained from Oriental Yeast and housed under specific pathogen-free conditions.

METHOD DETAILS

Generation of human lung normal and tumor organoids

Normal airway and alveolar organoids were established as previously reported.^{10,13} Derivation of lung tumor organoids from surgery and bronchoscopy specimens was performed as previously described.^{13,63} Briefly, lung tissues were washed with ice-cold PBS and cut into small pieces. The fragments were digested with Liberase TH (Roche) at 37°C for 30 min. Prior to plating, collected epithelia were washed with PBS supplemented with 10% fetal bovine serum (FBS) to inactivate digestive enzymes. Then, the epithelia were embedded in Matrigel (Corning) and cultured with the following medium.⁶³ Advanced Dulbecco's Modified Eagle's Medium/F12 was supplemented with penicillin/streptomycin, 10 mM HEPES, 2 mM GlutaMAX, 1 × B27 (Thermo Fisher Scientific), 10 nM gastrin I (Sigma), and 1 mM N-acetylcysteine (Wako, Japan) to prepare a basal culture medium. A complete medium was prepared by supplementing the basal culture medium with the following niche factors: 50 ng/mL mouse recombinant EGF (Thermo Fisher Scientific), 100 ng/mL human recombinant IGF-1 (BioLegend), 100 ng/mL human recombinant FGF-2 (Peprotech), 100 ng/mL mouse recombinant noggin (Peprotech), 1 mg/mL human recombinant R-spondin1 (R&D), 25% Afamin-Wnt-3A serum-free conditioned medium,⁶⁴ and 500 nM A83-01 (Tocris). Pleural effusion and ascites samples were centrifuged and washed 3 times with ice-cold PBS, and the sedimented cells were used for organoid culture. CTCs-derived organoids were established as previously described.⁶⁵ We isolated CTCs from 15 mL of blood samples drawn into heparin tubes at Keio University School of Medicine. The blood was incubated with 750 μ L RosetteSep CTC Enrichment Cocktail Containing Anti-CD36 (Stem Cell Technologies) for 20 min at room temperature, and then CTC enrichment was done using Ficoll-Paque PLUS (GE) by a negative selection. Isolated CTCs were washed and seeded in Matrigel. For sputum-derived organoid establishment, sputa were dissolved in semi-alkaline protease Suptazyme (KYOKUTO PHARMACEUTICAL INDUSTRIAL) for 15 min at room temperature, then the cells were washed with basal culture medium at 5–10 times and seeded in Matrigel. Plated organoids were maintained in a CO₂ incubator with 5% CO₂ and 20% O₂, and the media were changed every 3 or 4 days. To enrich LC organoids, we treated organoids with 3 μ M Nutlin-3 (Cayman Chemicals), or with 1 μ M pan-ErbB inhibitor (Merck Millipore) in the absence of EGF, IGF-1 and FGF-2. We added 10 μ M Y-27632 (FUJIFILM Wako Pure Chemical) for the first two days after passaging. To facilitate organoid establishment from LC tumors, we tested human recombinant FGF-7 (Peprotech), FGF-10 (Peprotech), HGF (Peprotech), neuregulin-1 (Peprotech), IL-6 (Peprotech), Wnt7B (Abnova) and DAPT (Sigma-Aldrich) at various concentrations but failed to promote culture efficiency. We routinely validate the uniqueness of each line to exclude possible contamination from other organoid lines and mycoplasma infection using RNA-seq. Once tumor-derived organoids were established, niche factors were subsequently removed to determine the minimal requirements of the niche factors. When the organoids survived without a given niche factor for at least 1 month, the organoids were judged to be independent of the niche factor. Each screening was carried out in duplicate or triplicate. When the organoids did survive but showed a declined growth

after the removal of a niche factor, we judged their niche factor dependency based on the viability after 3 months of culture. The bright-field image of each well was captured using a BZ-X800 digital microscope (Keyence), and the organoid area was automatically measured using the BZ-X800 Analyzer software (Keyence).

Xenotransplantation of lung tumor organoids

Prior to transplantation, the organoids were labeled with GFP by electroporation with a GFP-puro PiggyBac vector (System Biosciences) as previously described.⁶⁶ For each transplantation, LC cell clusters (equivalent to 1×10^5 cells) were resuspended in 10 μ L of cold Matrigel and injected into the subrenal capsule of a NOG mouse or the subcutaneous space of a BALB/c-nude mouse. At 2- or 3-months post-transplantation, mice were euthanized, and the grafts were isolated. The tumor size was measured using GFP fluorescence (Nikon Multi-zoom microscopy, LuminaVision software). The grafts were fixed for subsequent histological analyses. For Porcn-i-treatment experiments, tumor-bearing mice were randomized before treatment and treated with C59 (50 mg/kg, administered twice a day by oral gavage) as demonstrated in Figure 7C. To induce dnTCF4 in Dox-inducible dnTCF4 tumors, we treated tumor-bearing mice with oral administration of doxycycline (1 mg/mL) for 21 days after 2 months from xenotransplantation (Figure S7D).

Immunohistochemistry and *in situ* hybridization

Isolated xenografts were immediately fixed with 4% paraformaldehyde. The standard protocols for sectioning paraffin-embedded tissues and H&E staining were used. For immunostaining, mouse anti-NKX2-1 (Dako, M3575, 1:200), mouse anti-KRT7 (Dako, M7018, 1:1000), mouse anti-p40 (NICHIREI BIOSCIENCES, 418,171, 1:100), rabbit anti-KRT5 (Spring Biosciences, E13820, 1:200), rabbit anti-Synaptophysin (DAKO, A0010, 1:100), mouse anti-CD56 (DAKO, M7304, 1:200), rabbit anti-Chromogranin A (Dako, A0430, 1:1000), rabbit anti-HNF4 α (Cell Signaling Technology, 3113S, 1:100), and mouse anti- β -catenin (BD Biosciences, 610,153, 1:500) antibodies were used, with subsequent labeling by Alexa Fluor 488-, 568- or 647- conjugated anti-rat, -goat, -rabbit or -mouse antibodies (Thermo Fisher Scientific). Nuclei were counterstained with Hoechst 33,342 (Thermo Fisher Scientific). For *in situ* hybridization, we used an RNAscope 2.5 HD Kit (Advanced Cell Diagnostics), according to the manufacturer's instructions. Probes for *AXIN2* was designed by Advanced Cell Diagnostics. *PPIB* and *DapB* genes were used as positive and negative controls, respectively. Images were captured using a BZ-X710 digital microscope (Keyence) or a confocal microscope (SP8, Leica).

Drug testing

To analyze the response to sotorasib (Selleck) treatment, we plated single cell-dissociated organoids at a density of 1,500 cells per well and treated them at the indicated concentrations. Organoid viability assays were performed using CellTiter-Glo (Promega) on day 5 of treatment. The effect of the ALK inhibitor alectinib (Selleck) and BRAF inhibitor dabrafenib (Chemscene) was analyzed by treating single-cell passaged organoids with these compounds at 0.1 μ M. For EGFR pathway blockade, we used 1 μ M pan-ErbB receptor inhibitor (Merck Millipore).

DNA extraction

DNA was extracted from organoids and blood samples using the QIAamp Blood Mini Kit (QIAGEN) and treated with RNase Cocktail (Ambion) following the manufacturers' protocols. Three-micrograms of genomic DNA was fragmented.

Whole genome sequencing (WGS) analysis and variants call

We performed whole genome sequencing for 22 organoids and matched blood DNAs from 22 subjects using the NovaSeq 6000 platform (Illumina). Average sequencing depths were 33.2x for the organoids and 33.5x for control blood DNAs. We developed a WGS sequence analysis workflow called Tumor-GRAPPLer⁵⁷ that implements the features describe below and that is available on Github. Fastq files were aligned to the "no alt" version of human genome build GRCh38 with BWA-mem (version 0.7.17).⁴⁷ We called germline and somatic single-nucleotide, multi-nucleotide, and small insertion-deletion variants (SNVs, MNVs, Indels) using SAGE (version 2.8) (Somatic Alterations in Genome) from the pipeline of Hartwig Medical Foundation (HMF).^{52,67} We created a panel-of-normals (PON) VCF using SAGE run in PON mode for 149 Japanese reference samples to filter somatic variants. We annotated somatic variant VCFs with bcftools using mappability hdr and bed files from the HMF resource website, the PON vcf, dbSNP and ALFA (EAS and TOT AF and MAF) vcf, and ClinVar. We filtered VCFs for sites found in the PON, and further filtered to remove variant sites (MAF >0.01 and AF < 0.99) or likely fixed sites (AF \geq 0.99) based on the above dbSNP and ALFA population samples. We then annotated the using ANNOVAR⁵⁰ and SnpEff.⁵¹

We called structural variants (SVs) with GRIDSS (version 2.12.2)⁵⁰ using recommended workflow for preprocessing BAM files, splitting breakend assembly and then performing merged assembly and breakpoint/breakend calling. VCFs were then filtered using GRIDSS Post Somatic Software (GRIPSS) (version 1.11). Copy-number (CN) segment data were imported into R from PURPLE (version 3.1) (PURITY PLOidy Estimator) output and then further filtered and processed for use in downstream analysis programs.

We used software from HMF and developed our workflow based on the standalone GPL pipeline⁵⁴ to perform an integrated analysis of germline and somatic SNVs/MNVs/Indels, SVs, and copy-number alterations. AMBER 3.5 was run to generate a B-allele frequency (BAF) file from reference sample BAMs for 3,065,757 likely heterozygous SNV sites that we previously assembled. We then used COBALT (version 1.11) to calculated read depth ratios from reference normal and tumor BAMs. We then used germline and

somatic small variant VCFs, the GRIPSS filtered SV VCF, and the AMBER BAF file and COBALT read depth ratio files as input to PURPLE. PURPLE output was then input to LINX to cluster SVs into events and integrate SVs with germline and/or somatic driver variants.

Mutational signature analysis

We performed somatic mutation and CN signature analysis using SigProfiler with the filtered somatic variant VCFs after annotation by PURPLE, or for CN signature analysis in SigProfiler, we exported a tabbed text file of the processed CN segment data in ASCAT format (columns sample, chromosome, startpos, endpos, nMajor, nMinor). We generated somatic mutation and CN matrices using SigProfilerMatrixGenerator (version 1.2.0)⁵² and signature profiling was performed using SigProfilerExtractor (version 1.1.3)⁵³. Somatic mutation signature profiles were extracted for SBS96, DBS78, and ID83 signature types and decomposed to COSMIC 3.2 signatures (Table S2).

Whole exome sequencing (WES) analysis

For whole exome sequencing, 150 bp paired-end libraries were prepared using the SureSelect Human All Exon V6 kit (Agilent) according to the manufacturer's instructions. Cleaned fastq files were mapped onto the human reference genome version GRCh37 (hg19) using BWA-MEM (version 0.7.17). Data cleanup and variant detection were performed using Genome Analysis Toolkit (GATK, version 4.1.2.0). PCR duplicates were marked, and then base quality score recalibration was applied. Variant detection was performed using Mutect2. To remove germline variants, the detected variants were filtered by removing those detected with allele frequency of 0.1% or more in dbSNP or the Japanese germline variant database (the Human Genetic Variation Database).⁶⁸ Genotypes of 53,867 exonic germline variants registered in HapMap (version 3 release 3) were compared using CrosscheckFingerprints (GATK version 4.1.2.0).

RNA isolation

Organoids were cultured from single cells for 7–14 days in the identical culture medium containing Afamin-Wnt-3A, R-spondin-1, EGF, Noggin and A83-01. Engineered organoids overexpressing transcription factors were cultured with or without doxycycline for 10 days. RNA was extracted from organoids using the RNeasy Plus Mini Kit (QIAGEN) according to the manufacturer's instructions.

RNA sequencing of organoids

RNA quality was evaluated with an Agilent 2100 bioanalyzer (Agilent). Sequence library was prepared with TruSeq RNA Library Prep Kit v2 (Illumina) and sequenced with HiSeq X or NovaSeq 6000 (Illumina). Adaptors were removed from raw fastq files with cutadapt (version 1.18)⁴² and the reads were aligned to human genome (hg38) using STAR (version 2.6.1b).⁴³ The expression levels of the human genes in Ensembl release 81 were estimated with RSEM (version 1.3.3)⁵⁷. Differentially expressed gene analysis was performed using nbinomLRT in the R Bioconductor package DESeq2.⁴⁵ For gene set enrichment analysis (GSEA), read count data were normalized with size factors using DESeq2. GSEA was performed using the R Bioconductor package fgsea with 10,000 permutations.⁶⁹ IMA signature gene sets were used from previous report.⁷⁰

Re-analysis of the TCGA LUAD dataset

RNA-seq raw count data of TCGA LUAD cases were downloaded from Genomic Data Commons (GDC) Data Portal using the GDC Data Transfer Tool. Of these data, we used the data of the cases with quality-checked endpoint information.⁷¹ Genetic mutations of these cases were also obtained from the pan-cancer maf file in GDC Data Portal. From the count data, we removed transcripts with less than 10 read counts in all samples. The count matrix was then normalized using varianceStabilizingTransformation in DESeq2. The enrichment of WRd-related genes (WRd score) in each sample was calculated using simpleScore in the singscore R Bioconductor package.⁷² For this analysis, we used genes that were differentially expressed in WRd and WRi LUAD organoids (FDR <0.05 and absolute log2Fold change >1). The genes upregulated or downregulated in WRd organoids were used as the up gene set or the down gene set, respectively. The cutoff value of the WRd score for log rank test was determined using maxstat.test in the maxstat R package, and the difference in the overall survival between WR score-high tumors and -low tumors was analyzed with Kaplan-Meier method and log rank test using the Surv and survdiff functions in the survival R package.

Quantitative Real-Time PCR

Total RNA was isolated from organoids using an RNeasy Mini Kit (Qiagen), and genomic DNA was isolated using a DNeasy Blood and Tissue kit (Qiagen). RNA was subjected to reverse transcription using the High-Capacity RNA-to-cDNA Kit (Thermo Fisher Scientific) following the manufacturer's protocol. Quantitative RT-PCR was performed using fluorescent SYBR Green and Applied Biosystems 7500 Fast (Thermo Fisher Scientific). Human GAPDH was used as a housekeeping gene. Relative gene expression levels were calculated using the delta–delta Ct method. The primer sequences are shown in [key resources table](#).

Methylation microarray

For methylation analysis, 500 ng of genomic DNA was subjected to bisulfite conversion and applied to an Infinium MethylationEPIC microarray (Illumina) according to the manufacturer's instructions. We used the R Bioconductor package "wateRmelon" (version 1.20.3) to normalize signal and to obtain beta-value.⁴⁶ tSNE plot was performed using probes exhibiting large variance (M-value variance >4). Gene methylation level was obtained by selecting a probe with the largest negative correlation to the expression in probes mapped to the same gene loci (from 1.5 kbp upstream of the transcription start site to the transcription end site).

ATAC sequence of organoids

ATAC-seq was performed as previously described with minor modifications.^{73,74} For library preparation, organoids were dissociated into single cells and pretreated with DNase (Worthington) for 10 min at 37°C to remove DNA derived from dead cells. This medium was washed out, and the cells were resuspended in cold PBS. 50,000 cells were resuspended in 50 μ L of ATAC-seq resuspension buffer (RSB; 10 mM Tris-HCl pH 7.4, 10 mM NaCl, and 3 mM MgCl₂ in distilled water) containing 0.1% NP40, 0.1% Tween 20 and 0.01% digitonin, and were incubated on ice for 3 min. After lysis, 1 mL of ATAC-seq RSB containing 0.1% Tween 20 was added, and the lysate was centrifuged at 500 g for 10 min at 4°C. Supernatant was removed, and nuclei were resuspended in 50 μ L of transposition mix (25 μ L 2 \times TD buffer, 2.5 μ L Tn5 transposase, 16.5 μ L PBS, 0.5 μ L 1% digitonin, 0.5 μ L 10% Tween 20, and 5 μ L water) and incubated for 30 min at 37°C in Thermomixer shaking at 1000 rpm. Transposed DNA was purified using QIAGEN MinElute columns, and subsequently amplified with Nextera sequencing primers and NEB high fidelity 2x PCR master mix for 5–10 cycles. PCR-amplified DNA was purified using QIAGEN MinElute columns and sequenced on an Illumina HiSeq X with 150 bp pair-end reads. Each sample generated about 20–40 million mapped reads for the following analysis. For alignment, raw reads were trimmed using cutadapt⁴² and mapped onto hg38 using Bowtie2⁵⁸ with "–very-sensitive -X 2000" options. Samtools⁴⁸ was used to sort and remove reads that mapped to the mitochondria genome. Picard (<http://broadinstitute.github.io/picard/>) was then used to remove duplicates using the MarkDuplicates tool. Peak calling was performed using MACS2⁵⁹ with the parameters "–nomodel –call-summits –nolambda –keep-dup all –shift 75 –extsize 150." All peaks were resized to a uniform width of 501 bp, centered at the summit, and filtered by the ENCODE hg38 blacklist (<https://www.encodeproject.org/annotations/ENCSCR636HFF/>). Then, the peaks that overlapped the regions 1000 to +100 bp from the transcription start sites were excluded from any further analysis.

Global TF activity was analyzed using chromVAR.⁶² To find motif matches, we set bam files of each LC organoids and human_pwm_v2, which was curated from the cisBP database⁷⁵ as inputs for chromVAR "matchMotifs" function. We then computed the GC bias-corrected deviations and variability using the chromVAR "computeDeviations" and "computeVariability" functions, respectively. For downstream analysis, the value of bias corrected deviations of each TF and each sample was used. Motifs with a variance >2.25 were selected. Then, motifs which highly correlated with other motifs (Pearson correlation: R > 0.9) were discarded from further analysis.

Motif enrichment analysis was done using HOMER⁶⁰ against the whole genome background with a "–size 500" option. For centering peaks of the selected motifs, the HOMER function annotatePeaks.pl was used with a "–center –size 50" option. Then, motif-centered histograms were generated using deeptools⁶¹ with the computeMatrix and plotProfile tools.

Capillary-based immunoassay

For detection of phospho-ERK, organoids were grown under optimal growth culture conditions and subsequently cultured with or without EGF, IGF-1 and FGF-2, and with or without 1 μ M pan ErbB receptor inhibitor (Merck Millipore) for an hour. For confirmation of Dox-induced expression of NKX2-1, organoids were grown under optimal growth culture conditions and treated with doxycycline (50 ng/mL) for 2 days. Organoids were released from Matrigel using Cell Recovery Solution (Corning) lysed with Cell Lysis Buffer (#9803, Cell Signaling Technology) supplemented with a protease-phosphatase inhibitor cocktail (Thermo Fisher Scientific). Protein separation and detection were performed using an automated capillary electrophoresis system (Simple Western system and Compass software; proteinsimple). Antibodies against the following proteins were used; ERK-1/2 (#9102, Cell Signaling Technology, 1:50), phospho-ERK1/2 (T202/Y204) (#4370, Cell Signaling Technology, 1:50), NKX2-1 (#ab76013, abcam, 1:50) and β -actin (#A1978, Sigma, 1:50). Signals were detected with an HRP-conjugated secondary anti-mouse or anti-rabbit antibody and were visualized using the Compass software.

Gene manipulation of organoids

For gene knockout using CRISPR-Cas9, gene specific single-guide RNAs (sgRNAs) were cloned into the pX330-U6-Chimeric_BB-CBh-hSpCas9 vector⁴¹ (Addgene #42230). As we could not select *CDKN2A* knockout organoid clone with a specific niche condition or drug, we simultaneously introduced *TP53* and *CDKN2A* sgRNAs. Electroporated organoids were cultured with Nutlin-3 (3 μ M) to select *TP53* knockout clones. Then, stochastically introduced *CDKN2A* knockout was confirmed using Sanger sequencing. Biallelic introduction of frameshift mutations was confirmed using the TIDE web tool.⁴⁹ EGFR^{L858R} and KRAS^{G12V} cDNAs were PCR-amplified from reverse-transcribed RNA and were individually cloned into pLVSI-NEF1 α -IRES-ZsGreen1 (Takara #6191). The plasmids were co-transfected with packaging plasmids (psPAX2, Addgene #12260 and pMD2.G, Addgene #12259) into HEK293T cells using X-treme GENE 9 DNA Transfection Reagent (Roche). Transfected 293T cells were cultured in 10% FBS-containing DMEM penicillin/streptomycin to generate the lentivirus. For lentivirus infection, organoids were suspended in lentivirus suspension supplemented with 10 μ g/mL polybrene (Millipore), 10 μ M Y-27632 and 3% Matrigel and were centrifuged at 600 g, 32°C for 1 h.

Infected cells were incubated in 5% CO₂, 37°C for 6 h, washed with basal medium and re-embedded in Matrigel. Infected organoids were selected with a one-week treatment with 10 μg/mL blasticidin (Thermo Fisher Scientific). For NKX2-1 and dnTCF4 conditional overexpression, each cDNA was PCR-amplified from reverse-transcribed RNA and was cloned into the XLone-GFP vector⁴⁰ by replacing the GFP cassette using KpnI and SpeI digestion sites. XLone-GFP vector was co-electroporated with transposase (System Biosciences), and organoids were selected by a one-week treatment with 10 μg/mL blasticidin. Gene expression was induced with 50 ng/mL of Doxycycline. For knockout of *NKX2-1* knockout, we generated lentivirus expressing NKX2-1 sgRNA using lentiCRISPR v2-Blast (Addgene #83480), and organoids were infected with the lentivirus as mentioned above. Infected organoids were selected with a one-week treatment with 10 μg/mL blasticidin. sgRNA target sequence for *NKX2-1* are shown in [key resources table](#). Knockout was confirmed by biallelic introduction of frameshift mutations using the TIDE web tool ([Table S7](#)).⁴⁹

QUANTIFICATION AND STATISTICAL ANALYSES

Pairwise analyses for tumor volumes and gene expression was determined using Wilcoxon's rank-sum test or Welch's unpaired t test. The level of significance is indicated as the p value in each experiment. Asterisks in figures indicate the following: *, p value <0.05; **, p value <0.01; ***, p value <0.001; n.s., p value >0.05. The data are demonstrated as mean ± SEM. Graphs with statistical analysis were made with the R software. For further statistical details, refer to each figure legend.

Supplemental information

**Genotype-phenotype mapping of a patient-derived
lung cancer organoid biobank identifies NKX2-1-
defined Wnt dependency in lung adenocarcinoma**

Toshiki Ebisudani, Junko Hamamoto, Kazuhiro Togasaki, Akifumi Mitsuishi, Kai Sugihara, Taro Shinozaki, Takahiro Fukushima, Kenta Kawasaki, Takashi Seino, Mayumi Oda, Hikaru Hanyu, Kohta Toshimitsu, Katsura Emoto, Yuichiro Hayashi, Keisuke Asakura, Todd A. Johnson, Hideki Terai, Shinnosuke Ikemura, Ichiro Kawada, Makoto Ishii, Tomoyuki Hishida, Hisao Asamura, Kenzo Soejima, Hidewaki Nakagawa, Masayuki Fujii, Koichi Fukunaga, Hiroyuki Yasuda, and Toshiro Sato

Cell Reports

Supplemental Information

Genotype-phenotype mapping of a Patient-derived Lung Cancer Organoid Biobank Identifies NKX2-1-defined Wnt Dependency in Lung Adenocarcinoma

Toshiki Ebisudani, Junko Hamamoto, Kazuhiro Togasaki, Akifumi Mitsuishi, Kai Sugihara, Taro Shinozaki, Takahiro Fukushima, Kenta Kawasaki, Takashi Seino, Mayumi Oda, Hikaru Hanyu, Kohta Toshimitsu, Katsura Emoto, Yuichiro Hayashi, Keisuke Asakura, Todd A. Johnson, Hideki Terai, Shinnosuke Ikemura, Ichiro Kawada, Makoto Ishii, Tomoyuki Hishida, Hisao Asamura, Kenzo Soejima, Hidewaki Nakagawa, Masayuki Fujii, Koichi Fukunaga, Hiroyuki Yasuda, and Toshiro Sato

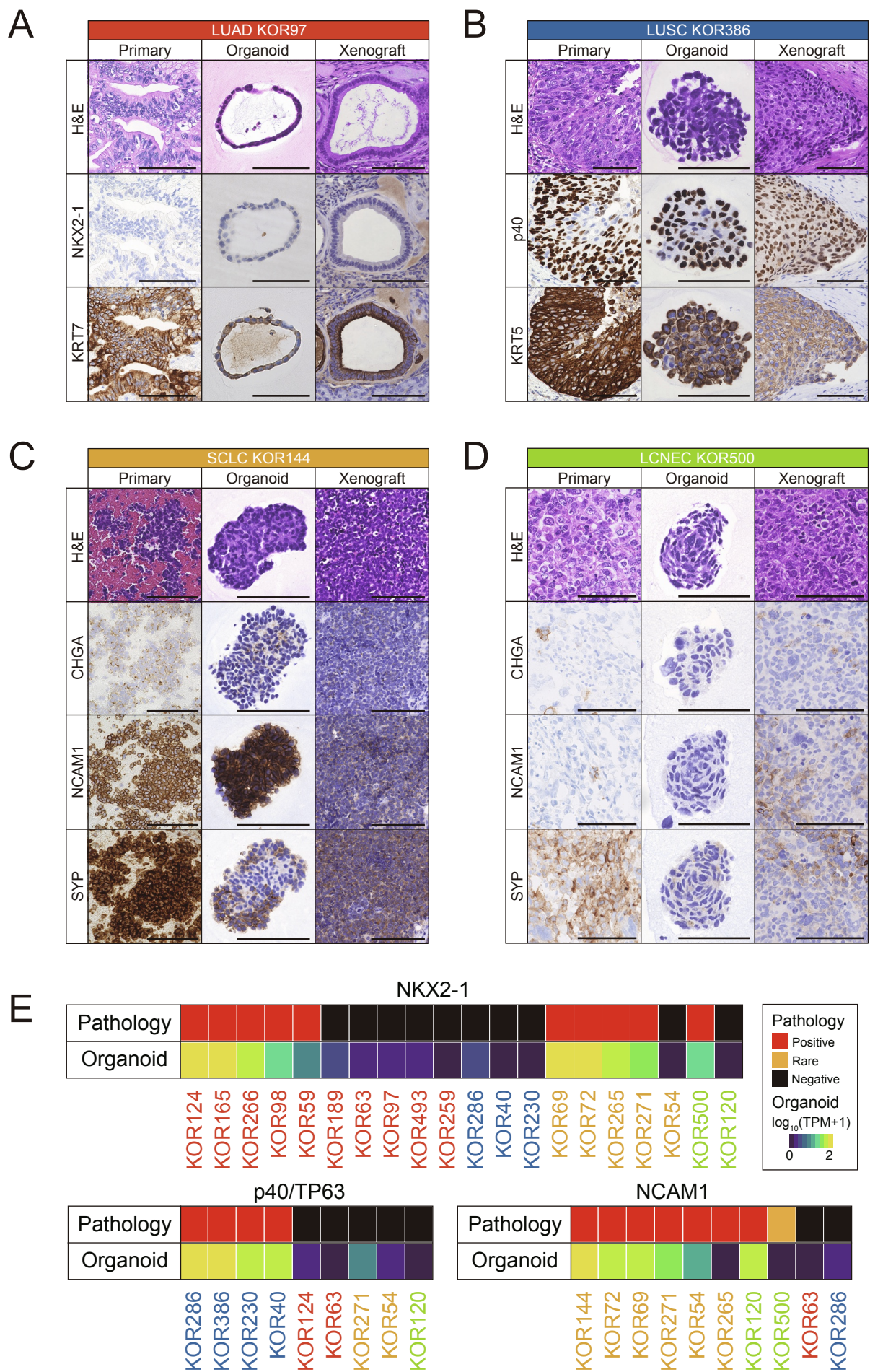


Figure S1

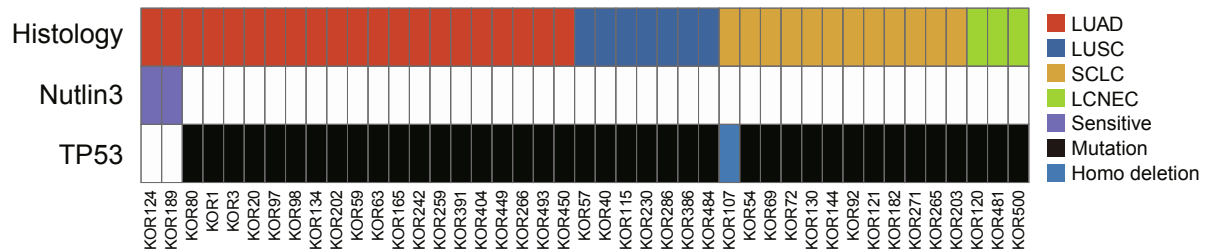
Figure S1. LC organoids preserve the original histological features in vitro and in Xenografts,

Related to Figure 1

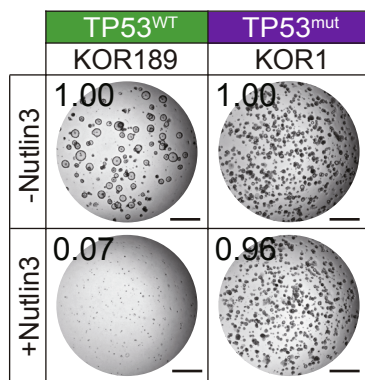
(A-D) Representative section images of the parental tumor (left), organoid (middle) and xenograft (right).

In all cases, original histological properties were preserved during culture and in xenografts. (E) Expression of NKX2-1, p40/TP63, and NCAM1 in organoids and parental samples. Transcript expression in organoids and immunoreactivity in parental samples are shown. Scale bar, 100 μm .

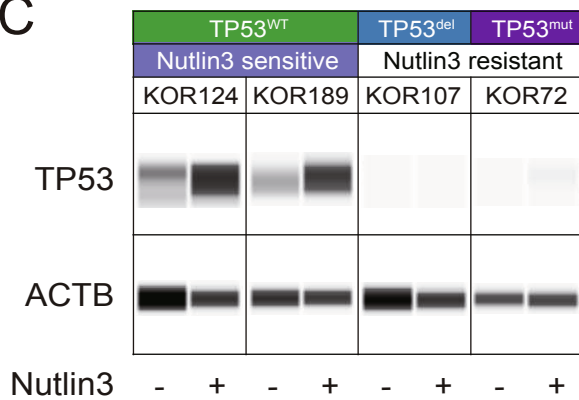
A



B



C



D

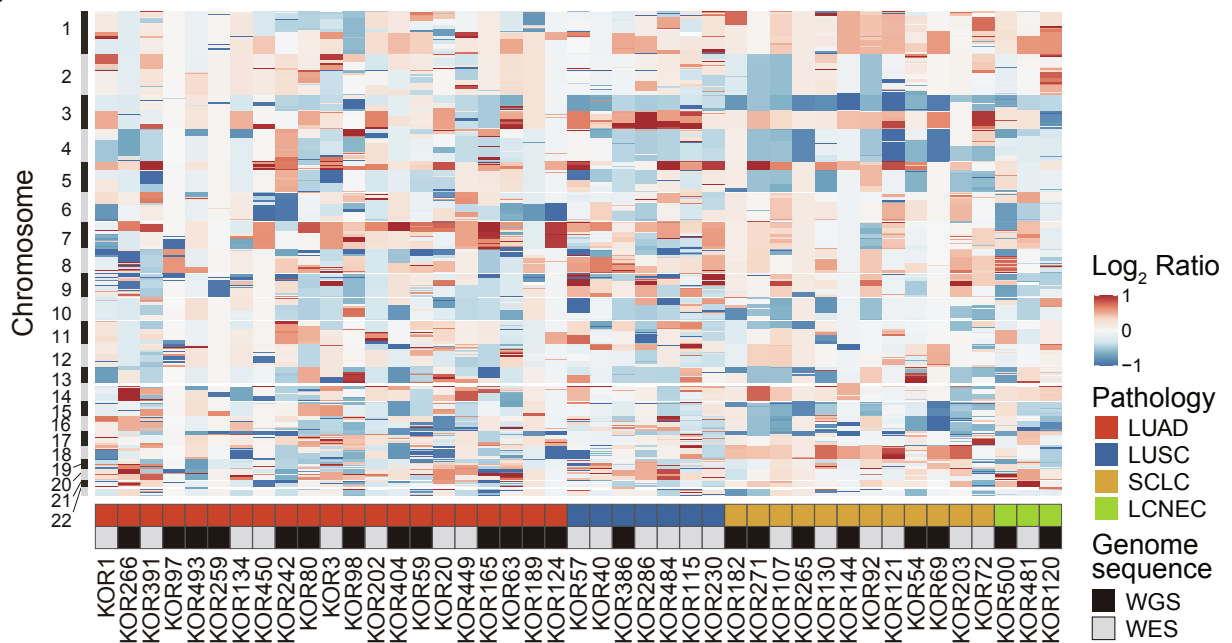
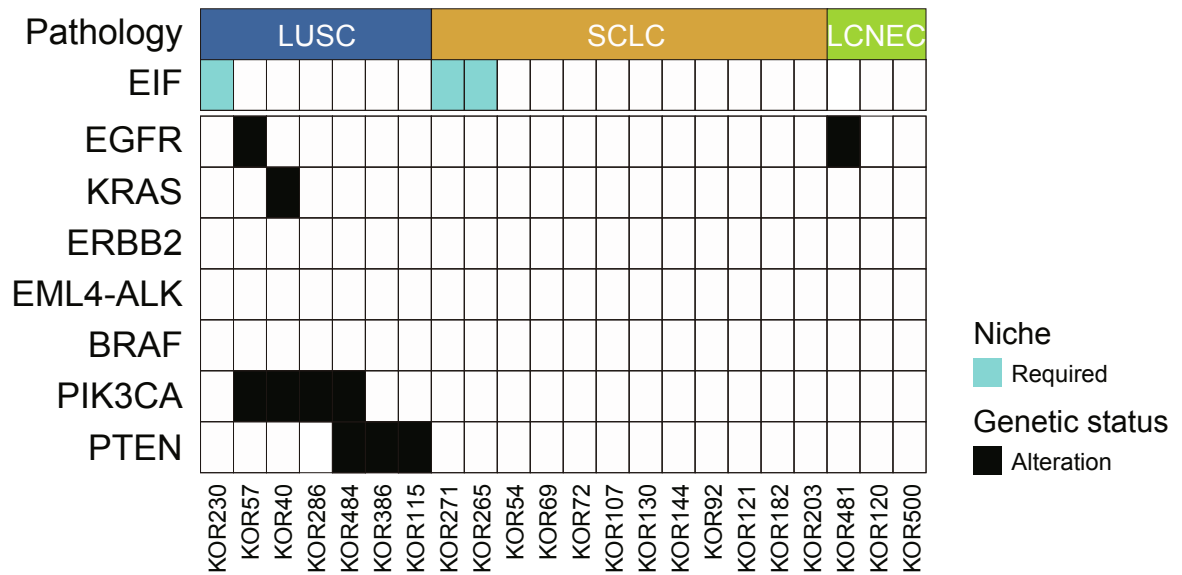


Figure S2

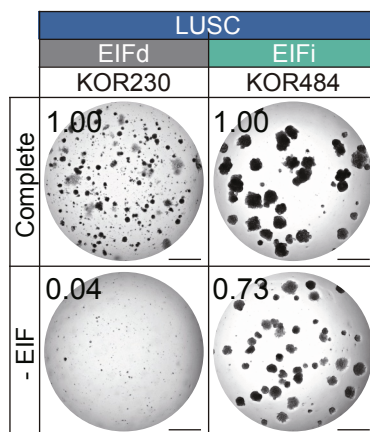
Figure S2. Nutlin-3 sensitivity and copy-number analysis of LC Organoids, Related to Figure 2

(A) Genetic alterations in *TP53* and resistance to Nutlin-3. Organoids with a genetic mutation or homozygous deletion are shown in black or blue, respectively, and those resistant to Nutlin-3 are shown in light purple. (B) Representative bright-field images of *TP53^{WT}* (left) and *TP53^{mut}* (right) organoid cultured with (top) or without (bottom) Nutlin-3. The mean organoid area relative to that of the control (-Nutlin-3) condition is presented. (C) An immunoassay demonstrating the loss of TP53 protein in organoids with a homozygous *TP53* deletion (*TP53^{del}*) and biallelic truncating *TP53* mutation (*TP53^{mut}*). Nutlin-3 treatment upregulated TP53 in wild-type organoids. (D) Copy number status of LTOL. The organoids were analyzed with WES (light gray) or WGS (black). Scale bar, 1 mm (B)

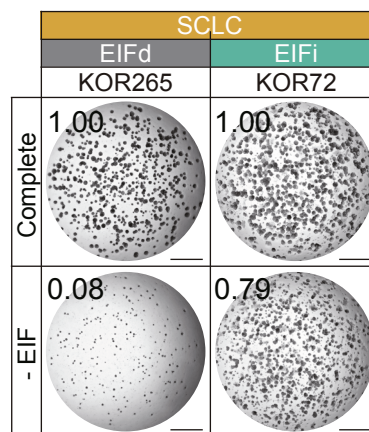
A



B



C



D

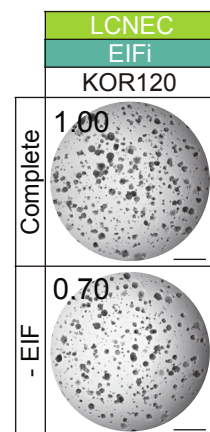


Figure S3

Figure S3. EGFR-RAS Signal Dependency in LUSC, SCLC, and LCNEC Organoids, Related to

Figure 3

(A) EIF dependency associated with RTK pathway-related genetic alterations in LUSC, SCLC and LCNEC organoids. (B-D) Growth of EIFd and EIFi LC organoids in EIF-included (Complete) and EIF-removed (-EIF) conditions (bottom). The mean organoid area relative to that of the complete condition is shown.

Heatmap showing the response of 50 cell lines to four conditions: Pathology, Wnt/Rspo, -Noggin+BMP4, and -A83-01+TGFβ. The cell lines are grouped by cancer type (LUAD, LUSC, SCLC, LCNEC) and niche (Required, Sensitive).

Pathology



- LUAD (Red)
- LUSC (Blue)
- SCLC (Orange)
- LCNEC (Green)

Niche

- Required (Cyan)
- Sensitive (Purple)

Cell Lines (Columns):

- KOR189, KOR97, KOR493, KOR63, KOR259, KOR80, KOR134, KOR3, KOR404, KOR266, KOR391, KOR124, KOR1, KOR242, KOR449, KOR450, KOR98, KOR20, KOR202, KOR59, KOR165, KOR230, KOR57, KOR484, KOR40, KOR115, KOR286, KOR386, KOR121, KOR107, KOR271, KOR265, KOR54, KOR69, KOR92, KOR72, KOR130, KOR182, KOR203, KOR144, KOR120, KOR481, KOR500

	β -catenin
APC ^{mut} LCNEC	
APC ^{WT} LUAD	


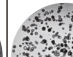
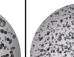
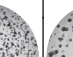

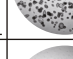




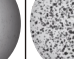
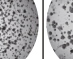
The diagram illustrates the genomic context and sequence of two genes, TP53 and CDKN2A, with a focus on a 2bp homo deletion in TP53 and a 2bp deletion in CDKN2A.

TP53: The gene structure shows Exon 9 (Ex9) and Exon 10 (Ex10). A 2bp homo deletion is indicated in the sequence between Ex9 and Ex10. The reference sequence (Ref) is shown as:

Ref → TGAATGAGGCCCTTGGAACTCAGGATGCC
 TGAATGAGGCCCTTGGAACTCAAGGATGCC
 (2bp homo deletion)

CDKN2A: The gene structure shows Exon 1 (Ex1) and Exon 2 (Ex2). A 2bp deletion is indicated in the sequence between Ex1 and Ex2. The reference sequence (Ref) is shown as:

Ref → AGCATGGAGCCTTCGGCTGACGGCTGGC
 AGCATGGAGCCTTCGGCTGGCTGGCTGGC (1bp del)
 AGCATGGAGCCTTCGGCTGGCTGGCTGGC (2bp del)

	Alveolar	TC	TCE	TCK
+Nutlin3				
-EIF				
-EIF+EI				

(kDa)	Alveolar		TC		TCE		TCK	
p-ERK								
44								
42								
t-ERK								
44								
42								
Ei	-	+	-	+	-	+	-	+





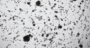



	Alveolar-2	TC-2	TCE-2	TCK-2
+WR				
-WR				

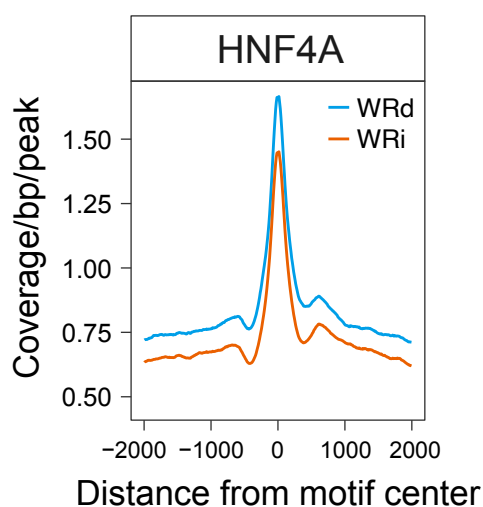
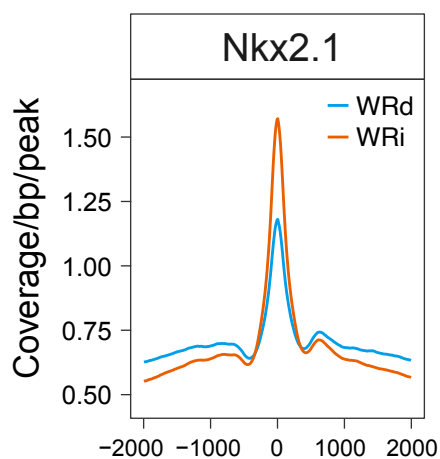
Figure S4

Figure S4. Niche Dependency and Gene Engineering of Normal Alveolar Organoid, Related to Figure

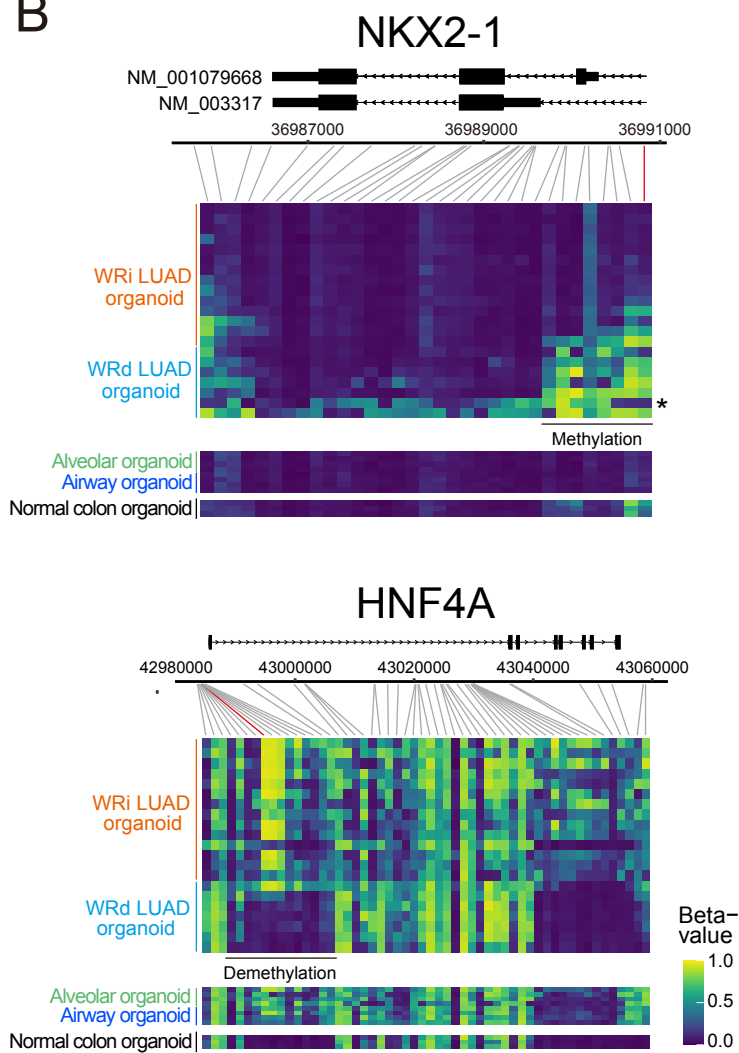
4

(A) WR dependency, BMP4 and TGF- β sensitivity of LC organoids. (B) b-catenin IHC of the subrenal xenograft samples of *APC^{mut}* LCNEC (KOR481) and *APC^{WT}* LUAD (KOR165) organoids. (C) Sanger sequencing confirmation of *TP53* (top) and *CDKN2A* (bottom) knockout in alveolar organoids. Black frames show sgRNA targets. (D) Representative images of normal and engineered alveolar organoids cultured with Nutlin-3 (top), WNRA (-EIF, middle), and -EIF plus Ei (-EIF+Ei, right) conditions. (E) Total and phospho-ERK expression following Ei treatment in normal alveolar and engineered alveolar (TC, TCE and TCK) organoids. (F) Representative images of an independent normal alveolar-2, TC-2, TCE-2, and TCK-2 organoids cultured with WR (top) or without (bottom) WR. Scale bar, 100 μ m (B), 1 mm (D, F).

A



B



C

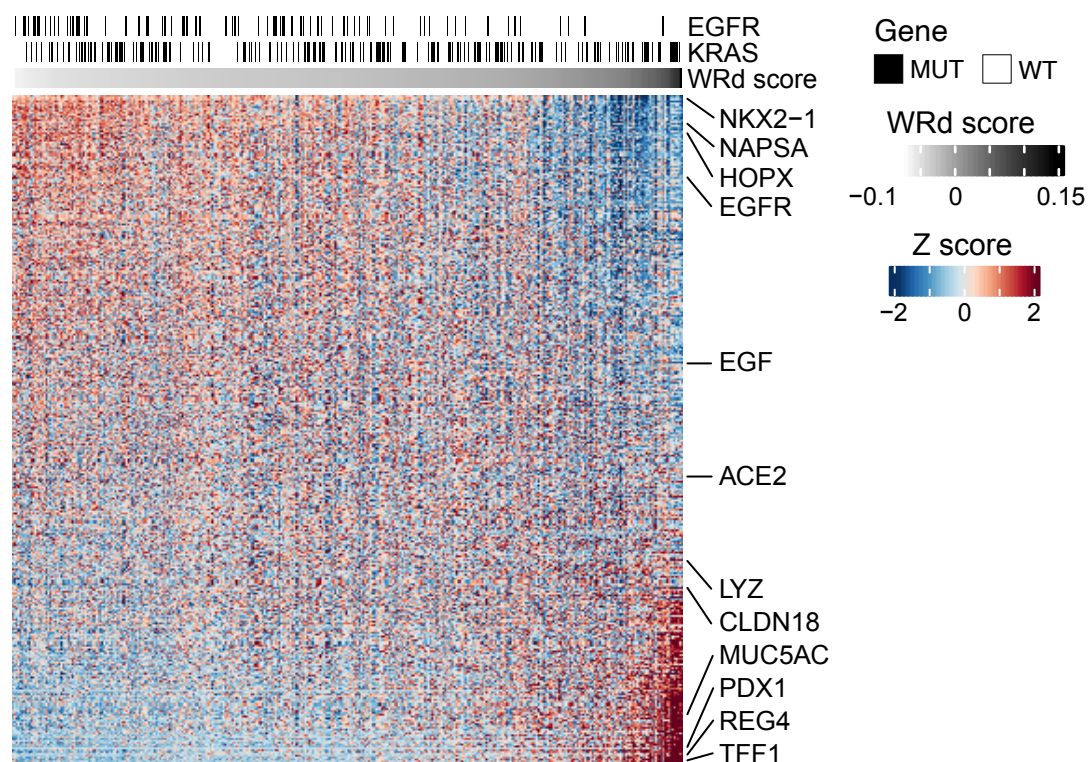


Figure S5

Figure S5. Epigenetic Regulation of NKX2-1 and HNF4A, Related to Figure 5

(A) Normalized ATAC-seq reads within 2 kb from the motif centers of *Nkx2.1* (top) and *HNF4A* (bottom). 7 WRd and 14 WRi LUAD organoids were analyzed. (B) Methylation beta values of the *NKX2-1* (top) and *HNF4A* (bottom) loci. WRd LUAD organoids show unique methylation of *NKX2-1* and demethylation of *HNF4A* compared to WRi LUAD and normal lung organoids. The methylation data of normal colon organoids is shown as negative and positive controls for *NKX2-1* and *HNF4A*, respectively. (C) The expression of genes differentially expressed between WRd and WRi organoids in the TCGA LUAD dataset. Or the differentially expressed genes, those with a standard deviation > 90 percentile in the TCGA dataset are shown. The samples were sorted according to the WRd gene enrichment score, and the genes were ordered based on the Spearman's correlation between the WRd gene enrichment score and normalized gene expression level.

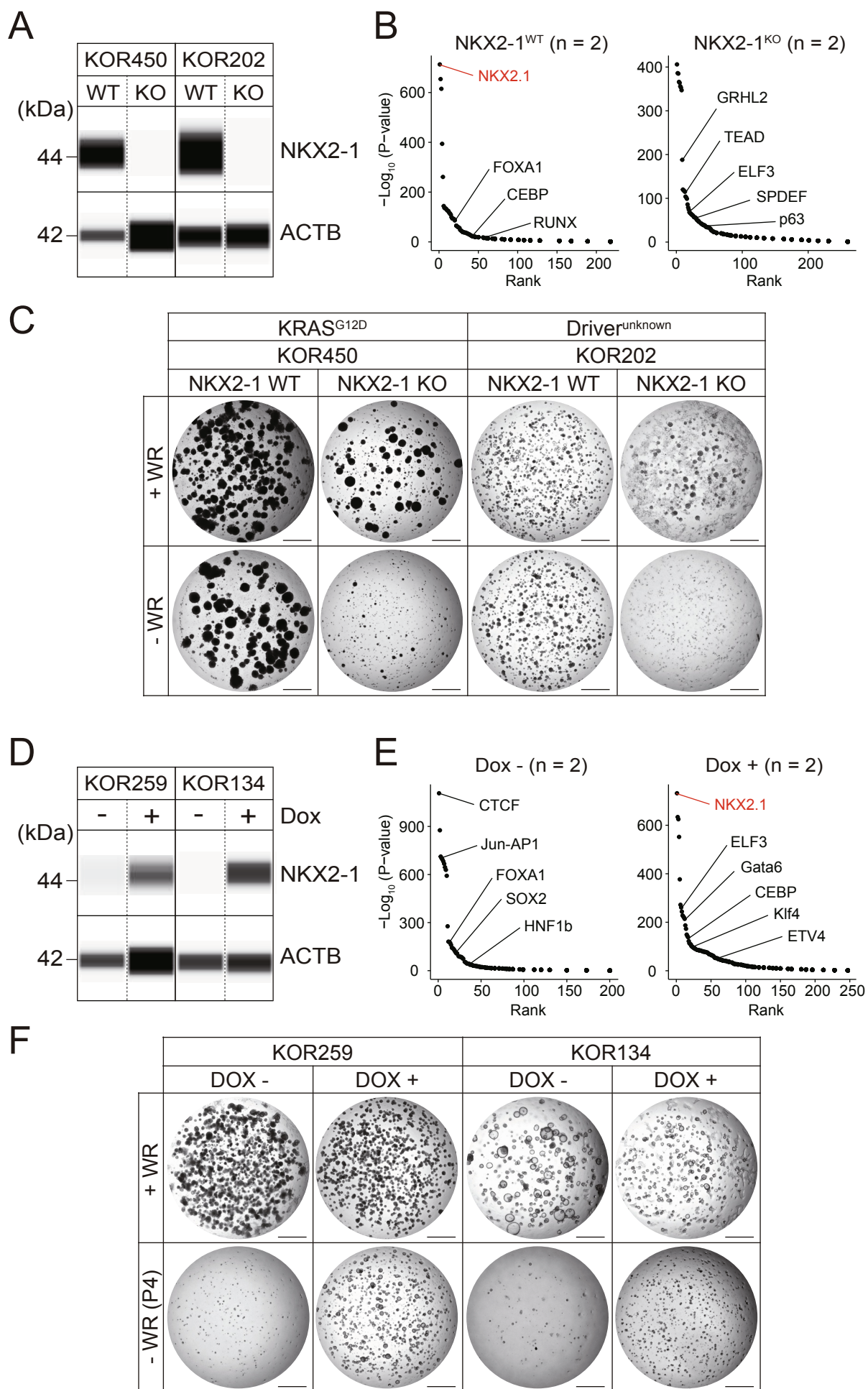


Figure S6

Figure S6. NKX2-1 Knockout or Overexpression Reverses WR Dependency in LUAD Organoids.,

Related to Figure 6

(A) An immunoassay demonstrating the loss of NKX2-1 in *NKX2-1* KO WRi LUAD organoids. (B) Enrichment of transcription factor motifs in 2 independent *NKX2-1^{WT}* (left) and *NKX2-1^{KO}* (right) WRi LUAD organoids. (C) Growth of *NKX2-1* WT and KO WRi LUAD organoids in +WR (top) and -WR (bottom) culture conditions. (D) Immuno-detection of NKX2-1 in NKX2-1^{OE} WRd LUAD organoids. (E) Enrichment of transcription factor motifs in 2 independent NKX2-1^{OE} WRd LUAD organoids without Dox (left) and with Dox (right). (F) Growth of NKX2-1^{OE} WRd LUAD organoids cultured with or without Dox in +WR (top) and -WR (bottom, passage 4) conditions. Scale bar: 1 mm (C, F).

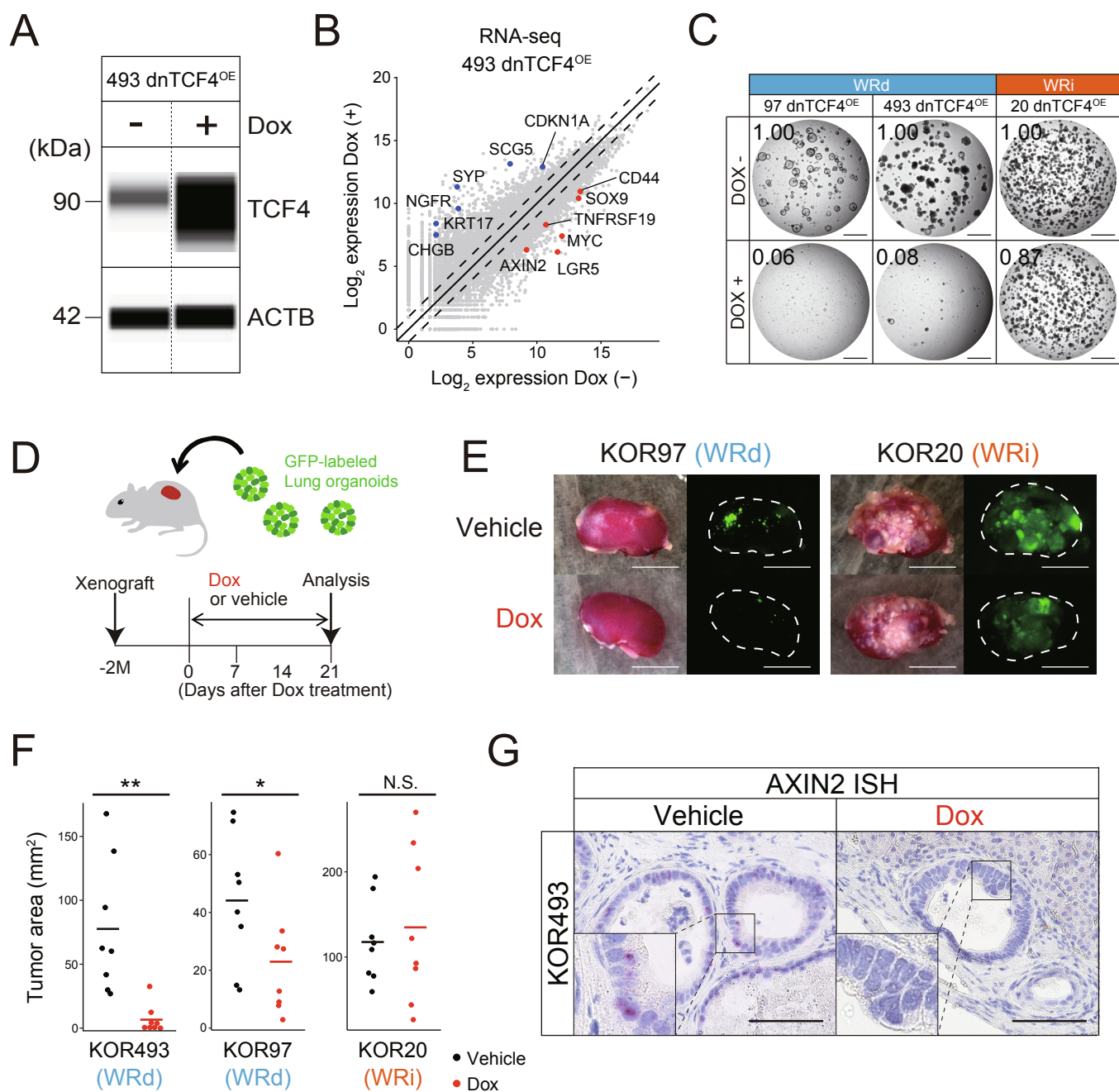


Figure S7

Figure S7. Wnt-Targeting is a Rational Therapeutic Strategy for the Treatment of NKX2-1 Negative LUAD, Related to Figure 7

(A) Induction of the dnTCF4 protein in dnTCF4^{OE} LUAD organoids with Dox. (B) Comparative transcriptome analysis of dnTCF4-induced and uninduced organoids. Representative Wnt target genes and genes downregulated by Dox treatment are highlighted in red and blue, respectively. (C) Representative images of WRd (left) and WRi dnTCF4^{OE} LUAD organoids cultured with (bottom) or without (top) Dox, and with WR. The mean organoid area relative to that of the DOX- condition is shown. (D) Subrenal transplantation of GFP-labeled LUAD organoids and doxycycline treatment. (E) Xenografts of WRd (left) and WRi (right) LUAD organoids treated with vehicle (top) or Dox (bottom). The kidney is outlined with dotted lines in fluorescent images. (F) The tumor area of grafts treated with vehicle (black) or Dox (red). Bars represent the mean area of the grafts. **p < 0.01, *p < 0.05, Wilcoxon's rank sum test. N.S., not significant. (G) *AXIN2* in situ hybridization in xenografts of WRd (left) and WRi (right) LUAD organoids. Scale bar: 100μm (G), 1 mm (C), 5 mm (E).

Table S1: Patient characteristics of LC Organoids, Related to Figure 1

KOR	Age	Gender	Smoking(BI)	Source	Histology	Subtype	Stage	T	N	M	Pre-treatment	Niche factor	Morphology	DNAseq	RNAseq	ATACseq	Methylation	EPIC	Candidate driver gene alterations
1	63	F	0	PE	LUAD	NA	IVA	3	3	1b	CBDCA/PEM, ERL, AFA, S-1, GEF, DTX, Nivo	A	Cystic	WES	+	+	+		TP53, CDKN2A, EGFR, MET, SETD2
3	63	F	0	PE	LUAD	NA	IIIa	1b	2	0	CDDP/DTX, CBDCA/PEM, Nivo	AN	Spherical	WES	+	+	+		TP53, CDKN2A, ERBB2
20	83	F	0	PE	LUAD	NA	IVA	4	3	1a	CBDCA/PEM/BEV, GEF, ERL, OSI, GEM/VNR	-	Mixed	WES	+	+	+		TP53, RB1, EGFR
59	58	F	0	CTNB	LUAD	Papillary	IVA	2a	0	1b	ERL, BEV, CDDP/PEM/BEV, OSI, GEM/VNR	-	Spherical	WGS	+	+	+		TP53, RB1, EGFR
63	61	M	740	surgery	LUAD	Solid	I B	2a	0	0	-	REIFN	Cystic	WGS	+	+	+		TP53, MET, SMARCA4
80	51	F	0	sputum	LUAD	NA	II B	2b	1	0	CBDCA/PTX/BEV, CDDP/PEM/BEV, Atezo	RA	Mixed	WES	+	+	+		TP53, CDKN2A, ERBB2
97	83	F	0	surgery	LUAD	IMA	II A	2b	0	0	-	RAN	Cystic	WGS	+	+	+		TP53, CDKN2A, KRAS, EP300
98	75	M	1000	surgery	LUAD	Solid	II A	2b	0	0	-	EIF	Spherical	WGS	+	+	+		TP53, CDKN2A, SETD2, ARID1A
124	70	M	860	BF	LUAD	NA	IVA	3	3	1b	-	A	Spherical	WGS	+	+	+		CDKN2A, BRAF, KEAP1
134	77	F	0	sputum	LUAD	NA	IVA	3	3	1b	-	R	Cystic	WES	+	+	+		TP53, CDKN2A, KRAS
165	83	M	0	surgery	LUAD	Acinar	I A2	1b	0	0	-	-	Spherical	WGS	+	+	+		TP53, CDKN2A, EGFR
189	61	M	1320	surgery	LUAD	IMA	II B	3	0	0	-	RAN	Cystic	WGS	+	+	+		CDKN2A, KRAS
202	78	M	1000	PE	LUAD	NA	IVA	2b	0	1a	-	-	Mixed	WES	+	+	+		TP53, CDKN2A
242	71	M	1200	PE	LUAD	NA	IVB	NA	3	1c	CBDCA/PEM	-	Spherical	WGS	+	+	+		TP53, CDKN2A, ALK
259	74	F	0	surgery	LUAD	Acinar	I A2	1b	0	0	-	RN	Mixed	WGS	+	+	+		TP53, CDKN2A, KRAS
266	78	M	36	surgery	LUAD	Acinar	I A3	1c	0	0	-	AN	Spherical	WGS	+	+	+		TP53, CDKN2A, EGFR
391	49	F	0	Ascite	LUAD	NA	IVB	1c	2	1c	RT, GEF, OSI, CBDCA/PEM/BEV	N	Spherical	WES	+	+	+		TP53, CDKN2A, EGFR
404	53	F	0	PE	LUAD	NA	IVA	2b	3	1b	ERL+BEV	AN	Spherical	WGS	+	+	+		TP53, RB1, EGFR, PTEN
449	52	F	0	PE	LUAD	NA	III B	2a	3	0	CDDP, DTX, PEM, DS8201a(Clinical trial), Atezo, S-1	A	Spherical	WES	+	+	+		TP53, RB1, ERBB2, ARID1A
450	74	M	1325	PE	LUAD	NA	III C	4	3	1a	CBDCA/PEM/Pembro, PEM, TS-1	A	Spherical	WES	+	+	+		TP53, CDKN2A, KRAS, STK11, SETD2
493	78	F	350	BF	LUAD	MP	IVB	3	1	1c	-	RAN	Cystic	WGS	+	+	+		TP53, CDKN2A, KRAS, NKX2-1
40	47	F	0	SC	LUSC	NA	IVA	2b	3	1b	Pembro	A	Spherical	WES	+	+	+		TP53, CDKN2A, KRAS, PIK3CA
57	63	F	0	PE	LUSC	NA	IVA	3	0	1b	ERL, CBDCA/S-1, OSI, Atezo	AN	Spherical	WES	+	+	+		TP53, CDKN2A, EGFR, PIK3CA
115	81	M	4000	sputum	LUSC	NA	IV	4	0	1	CBDCA/S-1, DTX, Nivo, VNR, Atezo	-	Spherical	WES	+	+	+		TP53, PTEN, PIK3CA
230	82	M	800	BF	LUSC	NA	IVA	1b	2	1b	-	REIFAN	Spherical	WES	+	-	+		TP53, STK11
286	79	F	400	BF	LUSC	NA	III A	1b	2	X	-	EIF	Spherical	WES	+	+	+		TP53, RB1, PIK3CA
386	65	M	900	surgery	LUSC	NA	II A	2b	0	0	-	A	Spherical	WGS	+	+	+		TP53, CDKN2A, PTEN
484	67	M	860	PE	LUSC	NA	IVB	4	3	1c	CBDCA/nabPTX/Pembro, DTX, TS-1	AN	Spherical	WES	+	+	+		TP53, PTEN, PIK3CA
54	83	M	800	PE	SCLC	NA	IV	NA	NA	1a	-	AN	Spherical	WGS	+	+	+		TP53, RB1
69	77	M	860	PE	SCLC	NA	IV	NA	NA	1a	CBDCA/VP-16	AN	Spherical	WGS	+	+	+		TP53, RB1
72	81	M	1000	BF	SCLC	NA	III B	2a	3	0	-	N	Spherical	WES	+	+	+		TP53
92	78	M	860	sputum	SCLC	NA	IV	NA	NA	1a	CDDP/VP-16, NGT	N	Spherical	WES	+	+	-		TP53, RB1, TP73
107	83	M	720	CTCs	SCLC	NA	I A3	1c	0	0	CBDCA/VP-16, AMR	N	Spherical	WES	+	+	+		TP53, RB1, EP300
121	65	M	600	sputum	SCLC	NA	IV	3	2	1	CBDCA/CPT-11, AMR, RT	WRAN	Spherical	WES	+	+	+		TP53, RB1
130	72	M	1650	PE	SCLC	NA	III B	3	2	0	CBDCA/VP-16, AMR, NGT	N	Spherical	WES	+	+	+		TP53, RB1, KEAP1
144	59	M	2460	BF	SCLC	NA	IVB	4	2	1c	-	-	Spherical	WGS	+	+	+		TP53, RB1, CREBBP
182	80	M	300	CTCs	SCLC	NA	III C	3	3	0	-	N	Spherical	WGS	+	+	+		TP53, RB1, CREBBP
203	58	M	960	CTCs	SCLC	NA	III B	2b	3	0	CDDP/VP-16, CBDCA/CPT-11, AMR	N	Spherical	WES	+	+	+		TP53, RB1
265	78	M	1800	surgery	SCLC	NA	I B	2a	0	0	-	EIFAN	Spherical	WGS	+	+	+		TP53, RB1, BRAF
271	72	M	1000	BF	SCLC	NA	IVB	2b	3	1c	CBDCA/nabPTX, DTX, Nivo, TS-1	EIFAN	Spherical	WGS	+	+	+		TP53, RB1, PTEN
120	55	M	585	surgery	LCNEC	NA	I A2	1b	0	0	-	AN	Spherical	WGS	+	+	+		TP53, PTEN
481	50	F	0	PE	LCNEC	NA	IVA	1b	3	1c	CBDCA/DTX, GEF, CBDCA/PEM/BEV, PEM, GEF, AFA, CBDCA+PEM, PEM+BEV, GEF, CBDCA+CPT-11	N	Spherical	WES	+	+	+		TP53, EGFR
500	47	M	540	Bone biopsy	LCNEC	NA	IVA	1a	1	1b	-	N	Spherical	WGS	+	+	+		TP53, RB1, SMARCA4

Abbreviations

Gender; M: male, F: female

Source; BF: bronchofiberscopy, CTNB: computed tomography-guided needle biopsy, PE: pleural effusion, CTCs: circulating tumor cells, SC: subcutaneous biopsy

Histology; LUAD: lung adenocarcinoma, LUSC: lung squamous cell carcinoma, SCLC: small cell lung carcinoma, LCNEC: large cell neuroendocrine carcinoma

Subtype; MP: micropapillary, IMA: invasive mucinous adenocarcinoma

Pre-treatment; CDDP: cisplatin, CBDCA: carboplatin, PEM: pemetrexed sodium hydrate, S-1: tegafur/gimeracil/oteracil potassium, DTX: docetaxel hydrate, PTX: paclitaxel, NabPTX: Nab-paclitaxel, VNR: vinorelbine ditartrate, VP-16: etoposide, CPT-11: irinotecan hydrochloride hydrate, NGT: nogitecan hydrochloride, AMR: amrubicin, GEM: gemcitabine, BEV: bevacizumab, GEF: gefitinib, ERL: erlotinib, OSI: osimertinib, Nivo: nivolumab, Pembro: Pembrolizumab, Atezo: Atezolizumab

Niche factor; W: Wnt, R: Rspodin, EIF: EGF/IGF-1/FGF-2/FGF10, N: Noggin, A: A83-01, -: no niche factor required